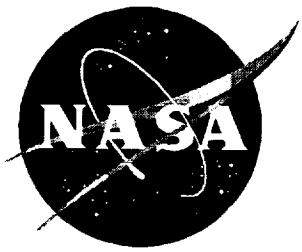

NASA Technical Paper 3480

Application of Navier-Stokes Code PAB3D With k-ε Turbulence Model to Attached and Separated Flows

Khaled S. Abdol-Hamid
Analytical Services & Materials, Inc. • Hampton, Virginia

B. Lakshmanan
Old Dominion University • Norfolk, Virginia

John R. Carlson
Langley Research Center • Hampton, Virginia

National Aeronautics and Space Administration
Langley Research Center • Hampton, Virginia 23681-0001

January 1995

The use of trademarks or names of manufacturers in this report is for accurate reporting and does not constitute an official endorsement, either expressed or implied, of such products or manufacturers by the National Aeronautics and Space Administration.

This publication is available from the following sources:

NASA Center for AeroSpace Information
800 Elkridge Landing Road
Linthicum Heights, MD 21090-2934
(301) 621-0390

National Technical Information Service (NTIS)
5285 Port Royal Road
Springfield, VA 22161-2171
(703) 487-4650

Introduction

Computational fluid dynamics (CFD) methods and advanced turbulence models are needed to predict propulsion aerodynamic effects in transonic and supersonic free-stream conditions. Analytical results are frequently used to supplement the experimental data in critical design decisions. Accurate prediction of the pressure distribution and the skin friction coefficient is paramount to the design of propulsion systems. In the area of propulsion integration, accurate predictions of boundary layer structure, skin friction, and flow separation by CFD methods are critical.

Two-equation turbulence models (ref. 1) offer several advantages over other approaches that compute practical flow problems. For example, algebraic models lack turbulence history-dependent nonlocal effects (through the convection and viscous diffusion of the Reynolds stress models), effects which are known to be important in determining the turbulence structure in complex flows. The numerical calculations that use the more advanced Reynolds stress models (refs. 2 and 3) require the solution of transport equations for each component of the Reynolds stress tensor in addition to solution of the Navier-Stokes equations; this approach requires tremendous computational time for three-dimensional flow problems. The transport equations for second-order models require closure approximations for higher order turbulence correlations with uncertain physical foundations. Large-eddy simulations (ref. 4) constitute three-dimensional time-dependent computations that require enormous computational time compared with traditional transport equation turbulence models. Moreover, the application of large-eddy simulations to practical flows is often hindered by the difficulties in modeling the turbulence near solid boundaries and the problem of defiltering the results in complex geometries.

Transport equations have been included in the standard, two-equation turbulence model of energy and dissipation rate (k-ε). (See ref. 1.) The k-ε equations can be applied to the near-wall region as well as far away from wall boundaries. For flow regions far away from solid boundaries, the high Reynolds number form of the model can be used; however, wall-damping functions must be used near wall boundaries.

Speziale (ref. 5) developed a nonlinear version of the k-ε model that broadened the range of linear model application but maintained most of the popular features (such as reduction to mixing layer theories for thin shear flows and the ease of application in existing Navier-Stokes solvers without a substantial increase in the computational time). Speziale developed the new model by making an asymptotic expansion subject to constraints of dimensional and tensorial invariance, realizability, and material frame indifference. The model thus obtained was shown to yield substantially improved predictions in incompressible turbulent channel flows and to yield normal Reynolds stress differences that give rise to secondary flows in square ducts. In the present research work, the nonlinear model developed by Speziale was modified to include additional terms that contribute substantially to the magnitude of Reynolds stresses near the wall boundaries.

For transonic and supersonic flow propulsion applications, the local density variation in standard incompressible models does not adequately duplicate the experimentally observed reduction in growth rate of the mixing layer with increasing convective Mach number. However, substantial progress has been made in the development of appropriate compressibility corrections to the transport equation turbulence models. (See refs. 6 and 7.) These corrections resulted from direct numerical simulation of homogeneous compressible turbulence. Notably, Sarkar et al. (ref. 6) recognized the importance of including compressible dissipation in the two-equation turbulence model when computing high-speed flows. A simple correction was proposed for compressible dissipation that can be included easily in the existing two-equation turbulence models. The standard model is recovered when the model constants for these corrections are assumed to be zero.

The objective of this study was to systematically investigate the effect of grid resolution, near-wall damping, and various turbulence models on the computed flow field. A general-purpose, three-dimensional, multiblock Navier-Stokes code (described and applied in refs. 8–10) was used in the present study. The flow solver contains the Baldwin-Lomax turbulence model, a two-equation k-ε turbulence model with various near-wall damping functions, and a nonlinear stress model for resolution of flow-field anisotropies. In addition, the code has a built-in performance module to compute quantities such as lift, drag, thrust, and discharge coefficients. During a typical numerical simulation, these quantities are constantly monitored to assess the performance of the propulsion system.

The computed results were compared with published experimental data for flow fields of increasing complexity. The geometries considered were a flat plate (ref. 11), 16° and 24° compression corners (ref. 12), a two-dimensional airfoil section (ref. 13),

and supersonic flow through a square duct (ref. 14). The flat plate was selected because it is the simplest of all the geometries for which the effects of various near-wall grid spacing, turbulence models, and damping functions can be tested. The compression corner and airfoil geometries represent the next level of flow complexity because these cases contain a separated flow region that interacts with a shock. In the square duct, a secondary flow structure develops perpendicular to the main flow and is mainly attributed to the flow-field anisotropy which is not simulated by linear (isotropic) models. Depending on the nature of the flow, either the space- or time-marching options in the PAB3D code can be used. Space-marching solutions were obtained for the flat plate and square duct geometries. Time-dependent options were used to investigate separated and transonic flow fields (compression ramp and airfoil geometries).

Symbols

$A^+, C_{\text{cp}}, C_{\text{wk}}$	constants in Baldwin-Lomax turbulence model
a	duct half-width, m
C_D, C_E	model constants for nonlinear model
C_F	average skin-friction coefficient, $\int_0^x C_f \, d_x$
C_f	local skin-friction coefficient, $\frac{\tau_w}{q_\infty}$
C_p	pressure coefficient
C_μ	turbulence viscosity coefficient for k-ε model, 0.09
c	airfoil chord length, m
c_d	section drag coefficient
c_l	section lift coefficient
D	duct width, cm
$\mathbf{E}, \mathbf{F}, \mathbf{G}$	convective terms in x, y, and z directions
$\hat{\mathbf{E}}, \hat{\mathbf{F}}, \hat{\mathbf{G}}$	flux terms in ξ, η, and ζ directions
$\mathbf{E}_v, \mathbf{F}_v, \mathbf{G}_v$	diffusion terms in x, y, and z directions
e	total energy, Pa
$\mathbf{F}_{\text{fric}}$	total vector skin-friction force, N
F_{kleb}	Klebanoff intermittency factor
$F(n)$	function in Baldwin-Lomax turbulence model
$F_{\max}$	maximum of $F(n)$
F_{wake}	wake function for Baldwin-Lomax turbulence model
f_μ	damping function for k-ε equations
H	Heaviside function
J	Jacobian of coordinate transformation, m^{-3}
k	turbulent kinetic energy, Pa
L_k	near-wall term for k equation
L_ε	near-wall term for ε equation
l	mixing length for turbulent viscosity, m
M	Mach number
M_t	turbulent Mach number
M_{t0}	cutoff turbulent Mach number for Wilcox model
n	normal distance from wall, cm
$\mathbf{N}(n_1, n_2, n_3)$	unit normal vector
n^+	law-of-the-wall coordinate, $\frac{n\sqrt{\rho_w \tau_w}}{\mu_w} = \frac{n \rho_w u_\tau}{\mu_w}$
$n_{\max}$	normal distance from wall at $F_{\max}$ location, cm
$\overline{P}$	production term for k-ε equations
Pr	Prandtl number, 0.75
Pr_t	turbulent Prandtl number, 0.9
p	pressure, Pa
$\mathbf{Q}$	conservative variable
$\hat{\mathbf{Q}}$	$= \frac{\mathbf{Q}}{J}$
q	heat flux
R_c	cell Reynolds number, $R_c = \frac{Un}{\nu}$
R_t	turbulent Reynolds number
R_x	Reynolds number based on streamwise distance from plate leading edge, $\frac{u_\infty \rho_\infty x}{\mu_\infty}$
$\mathbf{S}$	source term for Navier-Stokes equation
S_k	source term for k equation

S_ε	source term for ε equation
T	temperature, K
t	time, sec
U, V, W	velocity components in ξ, η, and ζ directions, m/sec
u, v, w	velocity components in x, y, and z directions, m/sec
u^+	law-of-the wall coordinate, $\frac{u}{u_\tau} = \frac{R_c}{n^+}$
u_τ	friction velocity, $\sqrt{\frac{\tau_w}{\rho}}$
x, y, z	spatial coordinates, cm
Γ	compressibility correction factor
γ	ratio of specific heat, 1.4
ΔA	incremental cell face area, m^2
δ	Kronecker delta and boundary layer thickness
ε	turbulent energy dissipation
θ	boundary layer momentum thickness, cm
κ	Von Kármán constant
μ	dynamic viscosity coefficient, m^2/sec
ξ, η, ζ	generalized coordinates as functions of x, y, z, and t
ρ	density, kg/m^3
σ_k	diffusion coefficient for k equation
σ_ε	diffusion coefficient for ε equation
τ_{ij}	Reynolds stress components, where i and j represent x, y, or z
τ_w	wall shear stress, $\mu \frac{\partial \mathbf{u}}{\partial \mathbf{n}}\Big\|_w$
ω	vorticity
Subscripts:	
cros	matching point for inner and outer boundary layer regions
e	edge of boundary layer
i	inner
max	maximum
min	minimum
o	outer
w	wall
x, y, z	x, y, and z derivatives
∞	free stream
Superscripts:	
L	laminar
T	turbulent
Abbreviations:	
k-ε1	k-ε model, Jones and Launder wall damping
k-ε2	k-ε model, Van Driest wall damping
k-ε3	k-ε model, Speziale et al. wall damping
RMS	residual mean square
WF	wall function

Experimental Configurations

Flat Plate

The supersonic data for this model were obtained for an insulated flat plate tested in the NASA Ames Research Center 6-inch Heat-Transfer Tunnel. The model was a flat surface 40.64 cm (16 in.) long and had a lower surface leading-edge chamfer of 15°; it spanned the width of the tunnel. (See ref. 11.) The leading edge was rounded to a radius of 0.0076 cm (0.003 in.). The static pressure orifices were 0.0343 cm (0.0135 in.) in diameter and were placed 2.54 cm (1 in.) from the side edges of the plate. Transition from laminar to turbulent flow was forced near the leading edge by a strip of lampblack 1.27 cm (0.5 in.) wide placed at the leading edge of the plate. Data were obtained at a free-stream Mach number of 2.5 and a tunnel total pressure of 204 kPa (30 psia). The Reynolds number based on the distance measured from the flat-plate leading edge ranged from 2.1×10^6 to 6.2×10^6.

Boundary layer measurements were made over a survey area 10.16 cm (4 in.) to 20.32 cm (8 in.) from the plate leading edge. The boundary layer measurements were performed with a total-pressure probe. The centerline of the probe was 0.0165 cm (0.0065 in.) above the surface when the probe was in contact with the plate surface. The probe had a rectangular external dimension of 0.2032 cm (0.080 in.) by 0.0330 cm (0.013 in.).

The free-stream Mach number varied by no more that 2 percent in the test section of the tunnel. That variation resulted in a skin-friction coefficient error of less than 2 percent; the total instrumentation error for the skin-friction coefficient was ±2.5 percent.

Compression Ramps

The compression ramp investigations were conducted in the 8 × 8-in. Supersonic Blowdown Tunnel at Princeton University. (See ref. 12.) The tunnel can provide a test duration of 30 sec to several minutes at stagnation pressures of 5.1 to 50.7 MPa (50 to 500 atm) over a Mach number range of 2.84 to 2.95, depending on which test sections are utilized. All of the models were tested in nearly adiabatic wall conditions. The particular data used for this study were obtained at a Mach number of 2.85 and a stagnation temperature of 262 K (472°R). The corresponding free-stream unit Reynolds number was 0.64×10^6 cm^{-1} (1.6×10^6 in^{-1}). The solid brass model consisted of a short upstream flat segment joined to a ramp that was 15.24 cm (6 in.) long by 16° or 24° compression corners. Sidewall fences were attached to each side of the ramp model to lessen the influence of the tunnel wall boundary layer on the compression corner flow. The boundary layer probe used for this study had a 0.0178-cm (0.007-in.) flat tip with 0.0076-cm (0.003-in.) orifices.

Pitot pressure tubes were used to make detailed flow-field surveys upstream of the compression ramps to determine the approaching flow properties. The displacement and momentum boundary layer thicknesses determined from these measurements were subsequently used to determine the computational inflow boundary conditions. The estimated errors were ±5 percent in the streamwise velocity component and ±10 percent in the skin-friction coefficient determined from the Preston tube measurements.

Subsonic Airfoil Section

The airfoil test case has an RAE 2822 airfoil contour (ref. 13) and is a subcritical design section with a trailing edge thickness of zero. The airfoil is 12.1 percent thick and is designed for a lift coefficient of 0.56 at a free-stream Mach number of 0.66. The data were obtained for a model with a 0.61 m (2 ft) chord and that spanned 1.83 m (6 ft) during an experiment conducted in the RAE 8 × 6-ft Transonic Wind Tunnel. (See ref. 13.) The tunnel is a continuous, closed circuit type that operates at a stagnation pressure range of 10 to 355 kPa (1.5 to 50 psi) with an average stagnation temperature of 307 K (552°R). Surface static pressure data, wake pitot and static pressure data, and boundary layer pitot and static pressure data were obtained for a variety of conditions with the transition fixed. Additionally, the oil-flow visualization technique was used to observe flow separation. An extensive description of the tunnel flow condition, wall interference, and instrumentation can be found in reference 13.

Square Duct

The experiment was set up in a continuous flow, open-circuit wind tunnel with a test section in the form of a square duct 50.8 cm (20 in.) long made of Plexiglas[1] material; it had a cross section of 5.08 cm (2 in.) at the duct inlet. A square brass constant-area duct with 2.54 cm (1 in.) on each side was placed within the outer Plexiglas duct. This "duct within a duct" configuration was built to ensure a clean starting condition for the inner duct flow by allowing the distorted flow that develops along the side walls of the outer duct nozzle to be bypassed through the annular space between the inner and outer ducts. The experiments were conducted at a free-stream Mach number of 3.9. The total pressure and total temperature at this location were 276 kPa (40 psi) and 300 K (540°R), respectively. A circular pitot tube with an outside diameter of 3.05 mm (0.12 in.) was used to obtain total pressure profiles at three streamwise locations; a flattened-tip probe with outside dimensions of approximately 2.5 × 6.6 mm (0.1 × 0.26 in.) was used to obtain boundary layer measurements. Wall shear stresses were calculated from measurements obtained with several differently sized Preston tubes resting on the wall. The experimental uncertainty in measuring the skin-friction coefficient is about 10 percent. Other pertinent details of the experimental setup and instrumentation are given in reference 14.

Theoretical Formulation

The governing equations of the Reynolds-averaged Navier-Stokes formulation include the conservation equations for mass, momentum, energy, and the equation of state. In the present study, the perfect gas law is chosen to represent the properties of air. For flow that contains turbulence, the Reynolds stresses are modeled using the eddy viscosity concept.

Turbulence models are essential for the realistic simulation of aerodynamics in the high Reynolds number regime. Two turbulence models were used

[1]Plexiglas: Rohm and Haas Co., Inc., Philadelphia, Pennsylvania.

for the current study: the Baldwin-Lomax algebraic turbulence model (ref. 15) and a two-equation k-ε turbulence model that follows the formulation of Jones and Launder. (See ref. 1.) The Navier-Stokes equations and the mathematical representations of the relevant turbulence models are described in the following sections.

Navier-Stokes Equations

The mass, momentum, and energy conservation equations of the Reynolds-averaged Navier-Stokes equations can be written in terms of generalized coordinates and in a conservative form as follows:

$$\frac{\partial \hat{\mathbf{Q}}}{\partial t} + \frac{\partial \hat{\mathbf{E}}}{\partial \xi} + \frac{\partial \hat{\mathbf{F}}}{\partial \zeta} + \frac{\partial \hat{\mathbf{G}}}{\partial \eta} = \mathbf{S} \tag{1}$$

where $\mathbf{S} = \{0, 0, 0, 0, 0\}^T$ for laminar or algebraic turbulence modeling. However, if a turbulence kinetic equation is used, the source term for the energy equation is replaced by the source term $-S_k$. In equation (1),

$$\hat{\mathbf{Q}} = \frac{\mathbf{Q}}{J}$$

$$\hat{\mathbf{E}} = \frac{1}{J}[\xi_x \mathbf{E} + \xi_y \mathbf{F} + \xi_z \mathbf{G}] - [\xi_x \mathbf{E} + \xi_y \mathbf{F} + \xi_z \mathbf{G}]$$

$$\hat{\mathbf{F}} = \frac{1}{J}[(\zeta_x \mathbf{E} + \zeta_y \mathbf{F} + \zeta_z \mathbf{G}) - (\zeta_x \mathbf{E}_v + \zeta_y \mathbf{F}_v + \zeta_z \mathbf{G}_v)]$$

$$\hat{\mathbf{G}} = \frac{1}{J}[(\eta_x \mathbf{E} + \eta_y \mathbf{F} + \eta_z \mathbf{G}) - (\eta_x \mathbf{E}_v + \eta_y \mathbf{F}_v + \eta_z \mathbf{G}_v)]$$

$$\mathbf{Q} = \begin{Bmatrix} \rho \\ \rho u \\ \rho v \\ \rho w \\ e \end{Bmatrix}$$

$$\mathbf{E} = \begin{Bmatrix} \rho u \\ \rho u^2 + p \\ \rho uv \\ \rho uw \\ (e+p)u \end{Bmatrix}$$

$$\mathbf{F} = \begin{Bmatrix} \rho v \\ \rho uv \\ \rho v^2 + p \\ \rho vw \\ (e+p)v \end{Bmatrix}$$

$$\mathbf{G} = \begin{Bmatrix} \rho w \\ \rho uw \\ \rho vw \\ \rho w^2 + p \\ (e+p)w \end{Bmatrix}$$

$$\mathbf{E}_v = \begin{Bmatrix} 0 \\ \tau_{xx} \\ \tau_{xy} \\ \tau_{xz} \\ -q_x + u\tau_{xx} + v\tau_{xy} + w\tau_{xz} \end{Bmatrix}$$

$$\mathbf{F}_v = \begin{Bmatrix} 0 \\ \tau_{xy} \\ \tau_{yy} \\ \tau_{yz} \\ -q_y + u\tau_{xy} + v\tau_{yy} + w\tau_{yz} \end{Bmatrix}$$

$$\mathbf{G}_v = \begin{Bmatrix} 0 \\ \tau_{xz} \\ \tau_{yz} \\ \tau_{zz} \\ -q_z + u\tau_{xz} + v\tau_{yz} + w\tau_{zz} \end{Bmatrix}$$

$$-q_x = \frac{1}{\gamma - 1}\left(\frac{\mu^L}{Pr} + \frac{\mu^T}{Pr_t}\right)\frac{\partial a^2}{\partial x}$$

$$-q_y = \frac{1}{\gamma - 1}\left(\frac{\mu^L}{Pr} + \frac{\mu^T}{Pr_t}\right)\frac{\partial a^2}{\partial y}$$

$$-q_z = \frac{1}{\gamma - 1}\left(\frac{\mu^L}{Pr} + \frac{\mu^T}{Pr_t}\right)\frac{\partial a^2}{\partial z}$$

In these equations, ρ is the density; u, v, and w are the velocity components in the x, y, and z directions, respectively; e is the total energy per unit volume; the pressure p is related to e by

$$p = (\gamma - 1)\left[e - \frac{1}{2}\rho\left(u^2 + v^2 + w^2\right)\right] \tag{2}$$

and, for example, $\tau_{xy} = \tau_{xy}^L + \tau_{xy}^T$. The laminar shear stress τ_{xy}^L may be expressed in the following forms:

$$\tau_{xx}^L = \frac{2}{3}\mu^L\left(2\frac{\partial u}{\partial x} - \frac{\partial v}{\partial y} - \frac{\partial w}{\partial z}\right)$$

$$\tau_{xy}^L = \mu^L\left(\frac{\partial u}{\partial y} + \frac{\partial v}{\partial x}\right)$$

$$\tau_{yy}^L = \frac{2}{3}\mu^L\left(2\frac{\partial v}{\partial y} - \frac{\partial w}{\partial z} - \frac{\partial u}{\partial x}\right)$$

$$\tau_{yz}^L = \mu^L\left(\frac{\partial v}{\partial z} + \frac{\partial w}{\partial y}\right)$$

$$\tau_{zz}^{L} = \frac{2}{3}\mu^{L}\left(2\frac{\partial w}{\partial z} - \frac{\partial u}{\partial x} - \frac{\partial v}{\partial y}\right)$$

$$\tau_{zx}^{L} = \mu^{L}\left(\frac{\partial w}{\partial x} + \frac{\partial u}{\partial z}\right)$$

The forms of the turbulent shear stress τ_{xy}^{T} for various turbulence models are described in the sections that follow. In the PAB3D code, all streamwise derivatives of the Reynolds stress ($\partial/\partial\xi$) have been omitted from equation (1) for computational economy. This formulation is known as the simplified Navier-Stokes equation. The remaining cross-stream derivatives can be numerically implemented either coupled or uncoupled. The uncoupled derivative is the thin-layer Navier-Stokes approximation. In all the results in this paper, the derivatives are uncoupled.

Baldwin-Lomax Turbulence Model

The Baldwin-Lomax model (ref. 15) is an algebraic two-layer turbulence model in which the turbulent eddy viscosity is evaluated as follows:

$$\mu^{T} = (\mu^{T})_{i} \qquad (n \le n_{\text{cros}})$$

$$\mu^{T} = (\mu^{T})_{o} \qquad (n > n_{\text{cros}})$$

where n is the normal distance from the wall and n_{cros} is the smallest value of n at which magnitudes of the viscosities at the inner i and outer o boundaries $(\mu^{T})_{i}$ and $(\mu^{T})_{o}$ are equal. The turbulent stress is determined from

$$\tau_{ij} = \mu^{T}\left[\left(\frac{\partial u_i}{\partial x_j} + \frac{\partial u_j}{\partial x_i}\right) - \frac{2}{3}\frac{\partial u_k}{\partial x_k}\delta_{ij}\right]$$

For the inner layer,

$$(\mu^{T})_{i} = \rho l^{2}|\omega| \tag{3}$$

where the mixing length for turbulent viscosity

$$l = 0.4n\left[1 - \exp\left(-n^{+}/A^{+}\right)\right] \tag{4}$$

and the vorticity

$$\omega = \sqrt{(u_y - v_x)^2 + (v_z - w_y)^2 + (w_x - u_z)^2} \tag{5}$$

For the outer layer,

$$(\mu^{T})_{o} = 0.0168 C_{\text{cp}}\rho F_{\text{wake}} F_{\text{kleb}}(n) \tag{6}$$

where F_{wake} is the smaller of $n_{\max}F_{\max}$ or $C_{\text{wk}}n_{\max}(u^2+v^2+w^2)_{\max}F_{\max}$. The term $n_{\max}$ is the value of n that corresponds to the maximum value of the model function F, $F_{\max}$, where

$$F(n) = n|\omega|\left[1 - \exp\left(-n^{+}/A^{+}\right)\right] \tag{7}$$

and the Klebanoff intermittency factor F_{kleb} is calculated by

$$F_{\text{kleb}} = \left[1 + 5.5\left(\frac{nC_{\text{kleb}}}{n_{\max}}\right)^{6}\right]^{-1} \tag{8}$$

The values of the constants appearing in equations (3)–(8) are listed in reference 15 as $A^{+} = 26$, $C_{\text{cp}} = 1.6$, $C_{\text{wk}} = 0.25$, and $C_{\text{kleb}} = 0.3$.

Two-Equation k-ε Turbulence Model

The Jones and Launder (ref. 1) formulation for the two-equation turbulence model uses k and ε as the principal variables. A modified form of the original Jones and Launder model is used in this study. This modified formulation is fully three dimensional, and the governing equations are written in a conservative form in terms of generalized coordinates. The governing equations can be cast in the same form as the Navier-Stokes equations (eq. (1)) with the following new definitions of the dependent variable and source terms:

$$\mathbf{S} = \begin{Bmatrix} S_\varepsilon \\ S_k \end{Bmatrix} \qquad \mathbf{Q} = \begin{Bmatrix} \rho\varepsilon \\ \rho k \end{Bmatrix} \qquad \mathbf{F} = \begin{Bmatrix} \rho v\varepsilon \\ \rho vk \end{Bmatrix}$$

$$\mathbf{E} = \begin{Bmatrix} \rho u\varepsilon \\ \rho uk \end{Bmatrix} \qquad \mathbf{G} = \begin{Bmatrix} \rho w\varepsilon \\ \rho wk \end{Bmatrix}$$

$$\mathbf{E}_v = \begin{Bmatrix} \mu_\varepsilon \frac{\partial \varepsilon}{\partial x} \\ \mu_k \frac{\partial k}{\partial x} \end{Bmatrix} \qquad \mathbf{F}_v = \begin{Bmatrix} \mu_\varepsilon \frac{\partial \varepsilon}{\partial y} \\ \mu_k \frac{\partial k}{\partial y} \end{Bmatrix} \qquad \mathbf{G}_v = \begin{Bmatrix} \mu_\varepsilon \frac{\partial \varepsilon}{\partial z} \\ \mu_k \frac{\partial k}{\partial z} \end{Bmatrix}$$

$$S_\varepsilon = C_1\overline{P}\frac{\varepsilon}{k} - C_2\rho\frac{\varepsilon^2}{k} + L_\varepsilon \qquad S_k = \overline{P} - \rho(1+\Gamma)\varepsilon + L_k$$

$$L_\varepsilon = \frac{2\mu^L\mu^T}{\rho}\left\{\left(\frac{\partial^2 u}{\partial x^2}\right)^2 + \left(\frac{\partial^2 u}{\partial y^2}\right)^2 + \left(\frac{\partial^2 u}{\partial z^2}\right)^2 + \left(\frac{\partial^2 v}{\partial x^2}\right)^2 + \left(\frac{\partial^2 v}{\partial y^2}\right)^2 + \left(\frac{\partial^2 v}{\partial z^2}\right)^2 + \left(\frac{\partial^2 w}{\partial x^2}\right)^2 + \left(\frac{\partial^2 w}{\partial y^2}\right)^2 + \left(\frac{\partial^2 w}{\partial z^2}\right)^2 + 2\left[\left(\frac{\partial^2 u}{\partial x\,\partial y}\right)^2 + \left(\frac{\partial^2 u}{\partial x\,\partial z}\right)^2 + \left(\frac{\partial^2 u}{\partial y\,\partial z}\right)^2 + \left(\frac{\partial^2 v}{\partial x\,\partial y}\right)^2 + \left(\frac{\partial^2 v}{\partial x\,\partial z}\right)^2 + \left(\frac{\partial^2 v}{\partial y\,\partial z}\right)^2 + \left(\frac{\partial^2 w}{\partial x\,\partial y}\right)^2 + \left(\frac{\partial^2 w}{\partial x\,\partial z}\right)^2 + \left(\frac{\partial^2 w}{\partial y\,\partial z}\right)^2\right]\right\} \tag{9}$$

$$L_k = 2\mu^L\left\{\left(\frac{\partial\sqrt{k}}{\partial x}\right)^2 + \left(\frac{\partial\sqrt{k}}{\partial y}\right)^2 + \left(\frac{\partial\sqrt{k}}{\partial z}\right)^2\right\} \tag{10}$$

Here, $\overline{P}$ is the fully three-dimensional production term defined as

$$\overline{P} = \tau_{xx}^T\frac{\partial u}{\partial x} + \tau_{yy}^T\frac{\partial v}{\partial y} + \tau_{zz}^T\frac{\partial w}{\partial z} + \tau_{xy}^T\left(\frac{\partial u}{\partial y} + \frac{\partial v}{\partial x}\right) + \tau_{yz}^T\left(\frac{\partial v}{\partial z} + \frac{\partial w}{\partial y}\right) + \tau_{zx}^T\left(\frac{\partial w}{\partial x} + \frac{\partial u}{\partial z}\right)$$

or is expanded to

$$\overline{P} = \mu^T\left\{\left(\frac{\partial u}{\partial y} + \frac{\partial v}{\partial x}\right)^2 + \left(\frac{\partial v}{\partial z} + \frac{\partial w}{\partial y}\right)^2 + \left(\frac{\partial w}{\partial x} + \frac{\partial u}{\partial z}\right)^2 + 2\left[\left(\frac{\partial u}{\partial x}\right)^2 + \left(\frac{\partial v}{\partial y}\right)^2 + \left(\frac{\partial w}{\partial z}\right)^2\right] - \frac{2}{3}\left(\frac{\partial u}{\partial x} + \frac{\partial v}{\partial y} + \frac{\partial w}{\partial z}\right)^2\right\} - \frac{2}{3}\rho k\left(\frac{\partial u}{\partial x} + \frac{\partial v}{\partial y} + \frac{\partial w}{\partial z}\right) \tag{11}$$

where

$$\mu^T = C_\mu\rho\frac{k^2}{\varepsilon} \qquad \mu_\varepsilon = \mu^L + \frac{\mu^T}{\sigma_\varepsilon} \qquad \mu_k = \mu^L + \frac{\mu^T}{\sigma_k} \qquad C_\mu = 0.09 f_\mu \tag{12}$$

$$C_1 = 1.44 \qquad C_2 = 1.92\left[1 - 0.3\exp\left(-R_t^2\right)\right] \tag{13}$$

$$\sigma_\varepsilon = 1.3 \qquad \sigma_k = 1.0 \qquad R_t = \frac{\rho k^2}{\mu_1\varepsilon} \tag{14}$$

$$\tau_{ij}^T = \mu^T\left[\left(\frac{\partial u_i}{\partial x_j} + \frac{\partial u_j}{\partial x_i}\right) - \frac{2}{3}\frac{\partial u_k}{\partial x_k}\delta_{ij}\right] - \frac{2}{3}\rho k\delta_{ij} \tag{15}$$

where i and j represent x, y, or z. The compressibility correction Γ and the damping function f_μ are described next.

Compressibility correction functions for k-ε model. High-speed turbulent flows have different characteristics than low-speed flows (incompressible flows). For example, the rate of spread of the shear layer in high-speed flows is much slower compared with that of low-speed flows. Several corrections for

this effect have been developed in the last few years. The two most widely used compressibility corrections are given below.

Sarkar et al. model (ref. 6):

$$\Gamma = M_t^2 \tag{16}$$

Wilcox model (ref. 7):

$$\Gamma = \left(M_t^2 - M_{t0}^2\right) H(M_t - M_{t0}) \tag{17}$$

where $H(x)$ is the Heaviside step function; M_t is the local turbulent Mach number defined as $\sqrt{k}/a$, in which a is the local speed of sound; and $\Gamma = 0$ for no compressibility correction.

Damping and wall functions for k-ε model. Solving wall-bounded flows requires the use of damping or wall functions. These functions adjust the turbulence viscosity near solid surfaces. The details of the damping and wall functions are given as follows.

Damping functions. The damping function f_μ adjusts the turbulent viscosity through the term C_μ. Far from the wall, $f_\mu = 1$; at the wall, $f_\mu = 0$. Three damping function forms were investigated in this study. They are referred to as k-ε1, k-ε2, and k-ε3 and are defined as follows.

The k-ε1 (Jones and Launder) form (ref. 1):

$$f_\mu = \exp\left[-\frac{3.41}{1 + (R_t/50)}\right] \tag{18}$$

The k-ε2 (Van Driest) form (as used by Nagano and Hishida, ref. 16):

$$f_\mu = 1 - \exp\frac{-n^+}{A^+} \tag{19}$$

Also, the quantity 2 in the near-wall term L_ε (eq. (9)) is replaced with $1 - f_\mu$.

The k-ε3 (Speziale, Abid, and Anderson) form (ref. 17):

$$f_\mu = \left(1 + \frac{3.45}{\sqrt{R_t}}\right) \tanh\frac{n^+}{70} \tag{20}$$

On any solid surface, the dissipation is set equal to L_k. Then, L_ε and L_k are set to zero.

Simple wall function form. Neither the Baldwin-Lomax nor the two-equation turbulence model (even with damping functions) is capable of producing accurate aerodynamic predictions based on minimal grid spacing normal to a wall with $n^+ \geq 5$. One way to achieve greater accuracy for grids with $n^+ \leq 50$ is through the use of the simple wall function (WF), although the use of this function is limited to the calculation of attached flows. The concept estimates the wall shear stress from law-of-the-wall coordinates n^+ and u^+ of the first cell from the wall (i.e., a surface cell). The equivalent turbulence viscosity at the wall is subsequently calculated from the estimated shear stress. (In the standard two-equation turbulence model, the turbulence viscosity at the wall is normally set to zero.) The wall function approach can be used to relax the restriction on n^+, which permits use of values up to 50. This approach typically speeds solution convergence rates by reducing the total grid count to describe the problem. The following steps describe the procedure for the wall function approach.

First, evaluate the surface cell Reynolds number as

$$R_c = \frac{\rho_w u n}{\mu_w}$$

The Reynolds number R_c can also be written as a function of the two nondimensional parameters u^+ and n^+ as $R_c = u^+ n^+$. Thus,

$$u^+ = \frac{R_c}{n^+} \tag{21}$$

A normalized velocity profile that relates u^+ and n^+ near a solid wall is described in many fluid mechanics textbooks. In a turbulent flow along a wall, Von Kármán and others have suggested that the flow should be divided into three zones governed by the value of n^+. Therefore,

$$u^+ = f(n^+) \tag{22}$$

In turbulent flow along a wall, the flow may be divided into three regions. First is the laminar sublayer in which the viscous stress is much greater than the Reynolds stress:

$$u^+ = n^+ \qquad (n^+ < 5) \tag{23}$$

The region immediately above the laminar sublayer is called the buffer zone. In this zone, the Reynolds and viscous stresses are of the same order:

$$u^+ = 11.5 \log_{10} n^+ - 3.05 \qquad (5 < n^+ < 30) \tag{24}$$

Farther from the wall, in the turbulent zone, the Reynolds stress is much greater than the viscous stress. Thus,

$$u^+ = 5.75 \log_{10} n^+ + 5.50 \qquad (30 < n^+) \tag{25}$$

In the solution to equations (21) and (22), n^+ is evaluated and the value of τ_w can be specified at the wall as follows:

$$\tau_w = \frac{\left[(\mu_w n^+)/n\right]^2}{\rho_w} \tag{26}$$

Then, because $\tau_w = (\mu^L + \mu^T)\frac{\partial u}{\partial n}\big|_w$, a corrected turbulent viscosity μ_w^T at the wall can be obtained. This corrected viscosity replaces the turbulent viscosity in all the transport equations.

Nonlinear k-ε model. The nonlinear k-ε model is obtained by adding quadratic terms to the linear model τ_{ij}^T to treat the mean velocity gradients. In equation (27), the first two terms on the right-hand side correspond to the linear model and the additional terms represent the contribution due to nonlinear effects. These changes to τ_{ij}^T in $\mathbf{E}_v$, $\mathbf{F}_v$, and $\mathbf{G}_v$ as well as $\overline{P}$ are as follows:

$$\begin{aligned}\tau_{ij}^T = -\overline{\rho}\overline{u_i'u_j'} = &-\frac{2}{3}\delta_{ij}\left(\mu^T\frac{\partial u_k}{\partial x_k} + \overline{\rho}k\right) \\ &+ 2\mu^T\overline{D}_{ij} + C_D C_\mu^2\frac{\overline{\rho}k^3}{\varepsilon^2} \\ &\times\left(\overline{D}_{im}\overline{D}_{mj} - \frac{1}{3}\overline{D}_{mn}\overline{D}_{mn}\delta_{ij}\right) \\ &+ C_E C_\mu^2\frac{\overline{\rho}k^3}{\varepsilon^2}\left(\overline{D}_{ij} - \frac{1}{3}\overline{D}_{mn}\delta_{ij}\right) \\ &+ \frac{2}{3}\mu^L\frac{k}{\varepsilon}\left(\frac{\partial\sqrt{k}}{\partial x_n}\right)^2 W_{ij}(n,m)\end{aligned} \tag{27}$$

$$W_{ij}(n,m) = -\delta_{ij} - \delta_{in}\delta_{jn} + 4\delta_{im}\delta_{jm} \tag{28}$$

$$\overline{D}_{ij} = \frac{\partial\overline{D}_{ij}}{\partial t} + \overline{v}\cdot\nabla\overline{D}_{ij} - \frac{\partial u_i}{\partial x_k}\overline{D}_{kj} - \frac{\partial u_j}{\partial x_k}\overline{D}_{ki} \tag{29}$$

where

$$\overline{D}_{ij} = \frac{1}{2}\left(\frac{\partial u_i}{\partial x_j} + \frac{\partial u_j}{\partial x_i}\right)$$

C_D and C_E are model constants, and $C_D = C_E = 1.69$.

This new nonlinear model differs from the original model developed by Speziale (ref. 5) by the addition of the last term on the right-hand side of equation (25). (See development in ref. 18.) Because both k and ε vary rapidly near solid boundaries, the additional term contributes significantly to the near-wall anisotropies. The nonlinear terms added to the standard model are important for the prediction of secondary flow in a square duct. The secondary flow develops in the cross-flow planes due to the cross-stream gradients of the Reynolds stress. For linear models the cross-stream gradient of the Reynolds stress difference is small; therefore, anisotropic flow features do not develop. However, the nonlinear models produce gradients of sufficient magnitude to develop the anisotropic or secondary flow feature. For $C_D = C_E = 0$, the linear model is recovered.

Performance Method

The performance method (refs. 19 and 20) obtains body forces through the application of the momentum theorem to a control volume that surrounds the model. The choice of surfaces over which the integration of forces is performed provides several options for calculation of the momentum and pressure forces on the model. The method used for this investigation integrates the mass flux and pressure forces over the model with

$$\mathbf{F} = \sum[\rho\mathbf{U}(\mathbf{U}\cdot\mathbf{N}) + (p - p_\infty)\mathbf{N}]\,\Delta A + \mathbf{F}_{\text{fric}} \tag{30}$$

where $\mathbf{F}$ is the total vector body force, ΔA is the area attributed to the cell face, and $\mathbf{N}$ is the unit normal vector of the cell face. The static pressure force on a solid wall is calculated by extrapolating the cell-centered static pressure to the wall surface and by assuming a zero velocity at the wall. The term $\mathbf{U}\cdot\mathbf{N}$ for solid walls vanishes as solution convergence is obtained.

Skin friction is calculated for the solid wall boundaries of the control volume. The viscous stress tensor used to determine the skin-friction force is calculated with only the velocity derivatives normal to the surface. The velocity gradients are determined by a two-point difference. The first velocity is a zero-magnitude vector positioned on the surface. The second velocity is the velocity at the cell center. The local shear stress tensor is constructed from the normal velocity gradients multiplied by the local viscosity. The viscosity was determined from Sutherland's formula (ref. 21) and used the static temperature at the local cell center.

Method of Solution

The simplified Reynolds-averaged Navier-Stokes equations and the associated turbulence models have been implemented in the computer code PAB3D. As mentioned previously, the numerical code has the option for either space- or time-marching solutions. In

particular, the space-marching option is well suited for supersonic flows with no embedded subsonic region or for flows in which pressure gradients are practically absent. The space-marching algorithm in the PAB3D code is also much more robust than the parabolized marching procedure. For cases in which the space-marching scheme criterion is met, the solution is as accurate as those obtained with the time-dependent algorithm. However, the space-marching procedure requires significantly less computer time (approximately a factor of 20 less) than does the time-dependent procedure.

Computational Procedure for Navier-Stokes Equations

The solver for the Navier-Stokes equations has been implemented in the PAB3D code with three different numerical schemes: the Van Leer flux-vector splitting scheme, the Roe flux-difference splitting scheme, and the space-marching scheme which is a modified version of the basic Roe scheme. These schemes are basically implicit and upwind and are constructed by using the finite volume approach. Only the inviscid portion of the flux vectors $\hat{\mathbf{E}}$, $\hat{\mathbf{F}}$, and $\hat{\mathbf{G}}$ are subjected to the splitting and upwind procedures. The diffusion terms of the Navier-Stokes equations are centrally differenced. A detailed description of the mathematical formulation for these schemes can be found in reference 8.

The flux-vector or flux-difference splitting is used in all three computational directions. The updated solution at each iteration is obtained by using an implicit procedure in the η and ζ mesh planes at each constant ξ value. The relaxation procedure in the ξ direction consists of a forward and backward sweep. This particular implementation strategy has an important advantage: because the metrics for the implicit procedure are only required for up to three planes, they are not stored for the entire grid domain. Instead, they are recomputed one plane at a time at the advancing front of the prevalent sweep direction. This approach requires less memory for the intermediate data structure. Typically, 20 words of memory are required for each grid point for moderate to large mesh sizes.

For a general time-dependent solution that uses the Van Leer or the Roe scheme, each iteration count contains a forward and backward sweep in the i direction, with one step of an implicit update of the solution in each of the cross planes. For several supersonic and subsonic flow conditions, the numerical scheme of Roe can be further simplified into a space-marching method as follows. The inviscid terms in the Navier-Stokes equation are discretized as an approximate Riemann problem. The interface flux in the streamwise direction is determined by separate terms that depend on the quantities on the upstream and the downstream sides of the interface. For fully supersonic or subsonic flow with a small pressure gradient, the information can travel only in the flow direction and is carried by the terms on the left-hand side. For these flow problems, the upstream effect carried by the terms on the right-hand side can be ignored when compared with the streamwise influences. A solution is obtained by performing sufficient implicit iterations in each plane until the convergence criteria are met. A solution in the entire computational domain is established in a single forward sweep. All solutions in this paper were obtained with either the standard or space-marching version of the Roe scheme.

Computational Procedure for k-ε Equations

The governing equations of the two-equation turbulence model are written as a pair of coupled transport equations in conservative form. In principle this model could be implemented with the Navier-Stokes equations as a set of seven coupled equations, or the model could be a separate implementation that is uncoupled from the Navier-Stokes equations. The fully coupled approach would result in an increase in the computational requirements and numerical stiffness. For this study, the k-ε equations are implemented uncoupled from the Navier-Stokes equations and from each other. Although the stiffness remains, it is alleviated to some degree by solving these two equations with a much smaller Courant-Friedrichs-Levy (CFL) number (usually 0.25 of the CFL number of the Navier-Stokes equations). The potential differences in the development of the flow over time and turbulence variable sets have not noticeably affected the convergence rate or the quality of the solutions.

The governing equations for the nonlinear model are the same as for the linear model except for the differences in the expressions for the Reynolds stresses. Because the additional nonlinear terms in the Reynolds stresses are not large, they are treated simply as added source terms in the code. However, the variables u, v, w, k, ε, and their first derivatives are already calculated for the linear model. The new variables that need to be calculated are the second derivatives. When the first and second derivatives are known, the nonlinear contribution of each component of the Reynolds stresses can be obtained. The nonlinear model required only 2 percent additional computational time at each time step and converged somewhat more slowly than the linear model.

This result is not surprising because the nonlinear k-ε model contains Reynolds stress relaxation terms that are dispersive rather than dissipative.

Multiblock Structure and Boundary Conditions

The PAB3D code uses a general multiblock grid topology to handle complex configurations. One-to-one, multiple-to-one, or general patched interfaces between the blocks are accepted by the code. An important feature of the PAB3D code is the partition concept in the streamwise direction. If different viscous stress models are employed within a block, the length of the block can be partitioned by means of the starting i index for each viscous stress model.

The boundary conditions often include inflow, outflow, free stream, solid walls, and geometrical symmetry. Five types of inflow and outflow boundary conditions are provided: Riemann characteristics, fixed inflow total temperature and pressure, completely fixed inflow parameters, constant pressure for subsonic outflow, and extrapolation for supersonic outflow. The Riemann characteristics boundary condition is used at free-stream boundaries. On a solid boundary, either a no-slip or an inviscid-slip boundary condition can be specified. Finally, the symmetry boundary conditions include mirror imaging across a plane and polar symmetry around an axis in any direction. A universal high-order symmetry boundary condition is used that was developed by Abdol-Hamid and Pao. (See appendix.) A logically simple control structure is required to direct the code execution for dimensions of the zones and blocks, solver options, connections between blocks, boundary conditions, time-stepping requirements, and turbulence models.

For the turbulence transport equations, either zero-order extrapolation or free-stream values are used for k and ε along the outer boundaries. If the flow is outgoing along the outer boundary, zero-order extrapolation is used. If flow entrainment is involved, then free-stream values are used along the outer boundaries and the values of k and ε are set such that a preselected nominal turbulence intensity is achieved. For all the results in this paper, this level is 1 percent of the flow velocity. For the inflow condition, laminar or algebraic turbulence model solutions were computed for the first few planes of the upstream blocks. In that flow region, the inflow profile for k takes the same shape as the vorticity profile except that it is multiplied by a specified value of maximum turbulence intensity. (See fig. 1.) When the k profile is known, the ε profile is obtained based on the hypothesis that production equals dissipation. These values of k and ε are used as boundary conditions for the k-ε blocks. On any solid surfaces in which the k-$\varepsilon 3$ model is applied, the dissipation ε_w is set equal to the value of L_k (eq. (10)) and k is set to zero. For k-$\varepsilon 2$ and k-$\varepsilon 2$, $\varepsilon_w = k_w = 0$.

Results and Discussion

We selected the well-established properties of flow over a flat plate to calibrate the different forms of the two-equation k-ε model utilized in this report. Mach numbers of 2 and 0.4 were selected for comparisons. Figure 2 shows law-of-the-wall solutions ($u^+ = u^*/u_\tau$ versus y^+) that use the k-$\varepsilon 1$ model for subsonic and supersonic flows at $R_\theta = 30\,000$, where u^* is defined as

$$u^* = \int_0^{u_\infty} \sqrt{\rho/\rho_w}\, du$$

Similar results were produced for both subsonic and supersonic flows. Then, the supersonic flow case was computed based on the Baldwin-Lomax turbulence model. (See fig. 3.) Both turbulence models agreed well with the theoretical curves. The k-$\varepsilon 1$, k-$\varepsilon 2$, and k-$\varepsilon 3$ turbulence models are compared (fig. 4) and all three models produce very similar results; that is, all three models predicted the Von Kármán constant of $k = 0.41$ within less than 2 percent. As expected, the different forms of the turbulence models give very similar predictions for this attached flow case.

Supersonic Flow on Flat Plate

In many cases, skin-friction drag represents a significant portion of the total drag of a supersonic vehicle. Accurate prediction of skin friction is essential for CFD applications in design and analysis. An insulated flat plate (ref. 11) operated at a Mach number of 2.5 over a Reynolds number range of 2.1×10^6 to 6.2×10^6 is modeled in the present study. Predicted velocity and average skin-friction predictions are compared with the experimental data. Both the Baldwin-Lomax and the k-ε turbulence models are used to predict the aerodynamic characteristics of this flow.

In the present analysis, a grid distribution of $71 \times 2 \times 81$ was used. The plate was 12 in. long, and the Reynolds number at the back of the plate was taken to be 6.2×10^6. First, the number of grid points was fixed at 81 in the k direction (normal to the wall) and the value of n^+ (nondimensional distance normal to the wall of the first grid) varied from 0.5 to 10. Figure 5 shows the streamwise velocity profile (at $x = 6$ in.) versus y/θ, where θ is the boundary layer momentum thickness. Both turbulence models predict reasonably well the overall boundary layer velocity development for $n^+ < 10$. However, the

k-ε1 model kept a very well-defined boundary layer development at $n^+ = 10$. On the other hand, the Baldwin-Lomax turbulence model gives a boundary layer development for $n^+ = 10$ similar to the one produced from a laminar solution. Figure 6 shows the average skin-friction predictions compared with experimental data as a function of Reynolds number. The Reynolds number is calculated based on the free-stream condition and the distance along the plate from the leading edge. The k-ε model average skin-friction prediction agreed well with experiment for $n^+ \leq 5$. However, the Baldwin-Lomax turbulence model gave poor predictions of C_F for $n^+ > 2.5$.

We performed a second set of computations by fixing $n^+ = 5$ and changing the number of grid points in the normal direction from 21 to 81 with the k-ε turbulence model. Figure 7 shows the comparison of experimental data for a Baldwin-Lomax solution computed with 81 grid points in the normal direction and the k-ε turbulence models solutions with varying numbers of grid points. The k-ε model produces similar results for all grid distributions computed. A similar result was obtained for the average skin friction on the plate. Thus, the distance of the first grid point from the wall is a very important parameter in predicting boundary layer flows, but the number of grid points is not important.

As shown in figure 6(a), the two-equation k-ε1 turbulence model fails to predict the wall skin friction for $n^+ > 5$. Figures 8 and 9 show the improvement obtained by using the simple wall function in k-ε1 to predict the streamwise velocity variation and skin friction at $n^+ = 10$ and 50, respectively.

The flat-plate test case was selected because it is the simplest of all the geometries for which the effects of various near-wall grid spacing, turbulence models, and damping functions can be easily tested. The results obtained with the k-ε turbulence model were much more accurate and consistent than those for the Baldwin-Lomax turbulence model for a wider range of n^+ (height of first grid line normal to solid surface). The n^+ value is a very important parameter for accurate prediction of boundary layer development in attached and separated flows. The number of grid points normal to the solid surface is not as important as a correct value of n^+.

16° and 24° Compression Ramps

The compression ramp is a very simple test case but contains complex aerodynamic characteristics. A flow of Mach 2.85 over 16° and 24° ramps has been computed and compared with data by Settles, Vas, and Bogdonoff. (See ref. 12.) The free-stream unit Reynolds number was 0.64×10^6 cm^{-1} (1.6×10^6 in^{-1}). For the 16° compression corner, both the Baldwin-Lomax and k-ε solutions were obtained. Only k-ε solutions were obtained for the 24° compression ramp because a steady-state solution could not be obtained from the Baldwin-Lomax turbulence model. Figures 10 and 11 show the computed wall pressures and local skin-friction distributions and comparisons with the experimental data for ramps at 16°. The calculations were done with a two-block configuration. The first block employs the Baldwin-Lomax turbulence model with $10 \times 2 \times 101$ grid points and sets the initial boundary conditions for the values of k and ε for the downstream second block. The second block spans the region from upstream of the separated flow region to the outflow boundary. This block had the dimensions $152 \times 2 \times 101$ and used the k-ε1 code option to simulate the flow field. Mesh sequencing is used to assess the effect of grid refinement on the computed results for the 24° compression ramp. The grid is setup such that the first index refers to the number of points in the j direction and the last index refers to the number of points in the k direction. The base grid, the half grid in the j direction, and the half grid in the j and k directions were selected to investigate the effect of grid resolution on the k-ε solutions. Only the fine grid (base grid) solution is shown for the 16° ramp. In the simulation of the 16° ramp (fig. 10(a)), good agreement was obtained in the prediction of the surface pressure distribution when both turbulence models were used. However, the skin-friction distribution produced different results. (See fig. 10(b).) For the 24° compression ramp, the computed pressure distribution was insensitive to the effect of grid refinement as shown in figure 11(a). However, the skin-friction results showed some sensitivity to the effect of grid refinement. (See fig. 11(b).) Good agreement was obtained for skin friction on the upstream portion of the ramp. The experimental data on the 24° ramp indicate a massive separation. The region between $x/\delta = -1.5$ and 1.0 where no experimental data were taken indicates the separation. The k-ε1 model was able to predict the attachment point accurately at $x/\delta \approx 0.03$, but it predicted the separation point slightly downstream of the experimental data at $x/\delta \approx -0.15$.

Airfoil Configuration RAE 2822

Experimental data for the RAE 2822 (case 10 at $R = 6.2 \times 10^6$) two-dimensional airfoil section are available in reference 13. The experimental data used for this comparison were at a free-stream Mach

number of 0.75 and at an angle of attack of 3.19 in tunnel coordinates. The computational results were performed at 2.8° to compensate for wall interference; the computation also included an angle-of-attack correction equation from reference 13. Six blocks are used in the present investigation and totaled 31 000 grid points. Two of these blocks were at the leading edge at $x/c \leq 0.03$, where the flow was assumed to be laminar as in the experiments. The outer boundary extent was $8c$, and no point vortex correction was included in the far field. The base grid, the half grid in the k direction, and the half grid in the k and j directions are selected to investigate the grid effect on the k-ε solutions. Figure 12 shows the comparisons among the three different grids and the experimental data. No significant differences are apparent between the half grid in the k direction and the base grid in the predicted pressure, velocity, and skin friction.

In the rest of this section we use the base grid for comparisons with the experimental data. The value for the first grid height in the computational mesh was $n^+ < 2$. Figures 13(a)–13(c) show the Baldwin-Lomax and k-$\varepsilon 1$ turbulence model predictions compared with the experimental data. In figure 13(a), both models predict a similar pressure coefficient C_p distribution, although k-$\varepsilon 1$ predicts the shock location slightly farther forward, which is in better agreement with the experiment. Figure 13(b) presents the local skin-friction predictions compared with the experimental data. The skin friction is normalized by the local boundary layer edge condition. Both models gave similar predictions for skin friction upstream of the shock. However, the Baldwin-Lomax turbulence model gave a much better prediction of the skin-friction data point downstream of the shock location. In general both models overpredicted the local skin friction to $x/c \leq 0.6$. Figure 13(c) shows the experimental streamwise velocity profile at $x/c = 0.9$ compared with predictions from both turbulence models. The k-$\varepsilon 1$ model provided a more accurate velocity profile than did the Baldwin-Lomax prediction. Different wall-damping function forms affect C_p, the velocity profile, and the local skin-friction prediction as shown in figure 14, which compares k-$\varepsilon 1$, k-$\varepsilon 2$, and k-$\varepsilon 3$. If $n^+ \leq 25$ is relaxed (fig. 15), again the k-$\varepsilon 1$ model (or any of the other forms) significantly overpredicts the local skin-friction values. However, use of the simple wall function brings the local skin friction within the range of the other models (predicted at $n^+ < 2$). All wall pressure distribution predictions with different wall-damping functions in the k-ε model and the simple wall function are summarized in figure 16. The k-$\varepsilon 1$ model ($n^+ = 25$) gives completely inaccurate predictions of C_p. However, the simple wall function with $n^+ \leq 50$ gives similar predictions compared with any of the other models operated at much smaller n^+ values (<2). Also, the simple wall function with a larger value of n^+ accelerated the convergence rate of the k-ε model as shown in figures 17 and 18. These figures show the L-2 norm of the residual RMS and of c_l as a function of the number of iterations, respectively. A solution with the wall function and $n^+ = 50$ was established in less than 2000 iterations, which was similar to the number of iterations required with the Baldwin-Lomax turbulence model. The following table summarizes the c_d and c_l predictions based on the different models and modifications.

Procedure	c_l	c_d
Experiment	0.743	0.0242
k-$\varepsilon 1$, $n^+ < 2$	0.720	0.0257
k-$\varepsilon 2$, $n^+ < 2$	0.764	0.0269
k-$\varepsilon 3$, $n^+ < 2$	0.772	0.0257
Baldwin-Lomax, $n^+ < 2$	0.756	0.0290
WF, $n^+ < 25$	0.730	0.0261
WF, $n^+ < 50$	0.736	0.0231
k-$\varepsilon 1$, $n^+ < 25$	0.364	0.0222

Supersonic Flow Through Square Duct

Numerical calculations that used linear and nonlinear k-ε turbulence models were carried out for supersonic flow through a square duct. Figure 19 shows a schematic of the known secondary flow pattern in square duct flows. The flow is symmetric about the y- and z-axes so only one quadrant of the duct flow was computed. A Mach number of 3.9 and a unit Reynolds number of 0.012×10^6 cm^{-1} (0.035×10^6 in^{-1}) were used with a 41×41 grid in the cross-flow plane and 251 grid points in the streamwise direction. Because the flow is complex, appropriate grid spacing near solid boundaries was maintained to ensure appropriate near-wall effects of k and ε. The first point located off the wall was $n^+ < 1$ and the grid was stretched in the normal direction by an exponential grid-stretching formula. Approximately 16 points were placed in each direction normal to the walls to resolve the boundary layer. The rest of the points in the normal direction were distributed uniformly between the edge of the boundary layer and the symmetry boundary.

Figures 20–24 show comparisons of the results obtained for the linear and nonlinear turbulence models and the experimental data. (See ref. 14.) Figure 20

presents the effects of linear and nonlinear turbulence models on the computed skin-friction distribution at $x/D = 50$. The skin-friction distribution obtained with the nonlinear model is in better agreement with the experimental data, whereas the linear model shows a monotonic increase in value for C_f with the spanwise coordinate. The nonlinear model captures the undulations observed in the experimental data with remarkable precision. These undulations represent the convecting effect of the secondary flow, corrections which were not predicted by the linear model.

Figure 21 shows the effect of two wall-damping functions (eqs. (18) and (20)) on skin-friction predictions when the nonlinear model is used. This result demonstrates that to obtain improved predictions, the nonlinear model has to be coupled with the appropriate damping function such as that developed by Speziale, Abid, and Anderson. (See ref. 17.) Previous studies with this near-wall model gave improved predictions in simple wall-bounded separated flows such as the backward-facing step. (See ref. 22.)

Figure 22 shows the effect of including compressibility corrections (eqs. (16) and (17)) on skin-friction predictions with the nonlinear model. Compressibility correction is clearly not needed for this case; the results obtained without a compressibility correction and with the Wilcox model (ref. 7) are both in close agreement with the experimental data. However, the Sarkar et al. model (ref. 6) gave lower values of C_f. These lower results are not surprising because the compressibility correction in reference 6 is applied to all regions of the flow and does not have a built-in mechanism to switch off near the wall boundaries where the compressibility effects are minimal. In contrast, the Wilcox compressibility correction has a switching function based on the local turbulence Mach number and turns off automatically in the regions with little or no compressibility.

Figure 23 shows the effect of grid resolution on the computed skin-friction distribution. These computations were performed for 21, 31, and 41 points in the normal direction but with the same streamwise grid spacing. When the mesh in the normal direction was refined, the stretching coefficient was progressively increased to obtain finer mesh spacing near the wall, but an identical number of grid points in the boundary layer was maintained. The points in the outer region increased by a factor of 3 in the transition from a coarse to a finer mesh.

Figure 24 shows the cross-flow velocity patterns computed with the linear and nonlinear models and the experimentally measured cross-flow pattern at $x/D = 50$. Dramatically improved results are obtained with the nonlinear model shown in figure 24(b). The results clearly show that the secondary flows (vortices) are symmetrical about the diagonal and rotate in opposite directions. These vortices are essentially driven by the gradients of the Reynolds stresses, which cannot be simulated with the linear models and which transport net momentum toward the corner of the duct. The computed cross-flow velocity vectors that are based on the nonlinear turbulence model agree well with the experimentally observed patterns. (See fig. 24(c).) In contrast, the linear model (fig. 24(a)), predicts a unidirectional flow because the turbulence model cannot adequately represent the flow physics.

Concluding Remarks

A systematic investigation was conducted to assess the effect of grid resolution and various near-wall damping functions in the turbulence model of kinetic energy (k) and dissipation rate (ε) on the computed flow field of several aerodynamic configurations. The computed results were compared with the available experimental databases. The geometries considered in the present study were a flat plate, 16° and 24° compression corners, a two-dimensional airfoil section, and supersonic flow through a square duct. In addition, a nonlinear k-ε turbulence model was used to predict the aerodynamic characteristics of supersonic flow through a square duct, and the effect of compressibility corrections was investigated. Skin-friction, pressure, and velocity distributions were reasonably predicted with the two-equation turbulence model in its different forms.

The flat-plate test case was selected because it is the simplest of all the geometries for which the effects of various near-wall grid spacing, turbulence models, and damping functions can be easily tested. The results obtained with the Jones and Launder turbulence model (k-ε1) were more accurate and consistent than those for the Baldwin-Lomax turbulence model for large n^+ (height of first grid line normal to solid surface). The number of grid points normal to the solid surface is not as important as a correct value of n^+. Use of the simple wall function with the k-ε turbulence model allowed the use of coarser grids in which $n^+ \leq 50$ but which maintained reasonably accurate predictions of skin friction.

The compression corner and airfoil geometries represent the next level of flow complexity because these cases contain separated flow regions that interact with a shock. A flow of Mach 2.85 over 16° and 24° compression ramps was computed and compared with the experimental data. For the case of

16° ramp, good agreement was obtained in predicting the surface pressure and the skin friction upstream of the ramp. The 24° ramp had a massive separated flow region. The k-ε1 model accurately predicted the reattachment point but predicted the location of the separation point slightly downstream of the experimental data.

For the airfoil geometry, the k-ε model with Jones and Launder damping function (k-ε1) and the Baldwin-Lomax turbulence model gave similar pressure coefficient distributions, although the k-ε1 model predicted the shock slightly farther, in better agreement with the experiment. Both models also yielded a similar prediction for skin friction upstream of the shock. The simple wall function with the k-ε1 turbulence model at large values of n^+ brought the local skin friction within the range of the predictions obtained for other models (predicted at $n^+ < 2$). Also, a larger n^+ accelerated the convergence rate of the k-ε model. Comparisons were also made between the models of Jones and Launder (k-ε1), Van Driest (k-ε2), and Speziale et al. (k-ε3). All models predicted similar pressure distributions, but use of different forms of the damping function yielded significantly different skin-friction predictions upstream of the shock. In general, the k-ε1 model most accurately predicted the overall features of the flow field.

For the test case that featured square duct geometry, a secondary flow structure developed in the direction perpendicular to the main flow. The skin-friction distribution with the nonlinear k-ε3 turbulence model was in better agreement with the experimental data, whereas the linear k-ε3 turbulence model produced a monotonic increase in the local skin friction with the spanwise coordinate. The nonlinear model clearly captured the major trends observed in the experimental data and flow-field features. The undulations that were observed represent the convecting effect of the secondary flow, undulations which were not predicted by the linear turbulence model. The near-wall damping function developed by Speziale et al. (k-ε3) helped to yield better prediction of the skin-friction distribution than that of Jones and Launder (k-ε1) for this case. The compressibility correction of Wilcox performed better than that of Sarkar et al. for this case because the former has a built-in mechanism to switch off near the wall where compressibility effects are small.

This investigation provided significant insight into the applications of turbulence models in the prediction of attached and separated flows. Comparisons of grid effects and the use of different turbulence models indicate that the k-ε turbulence model can be used successfully to predict these flows.

NASA Langley Research Center
Hampton, VA 23681-0001
October 26, 1994

Appendix

Universal High-Order Symmetry Boundary Condition for Navier-Stokes Codes

A universal symmetry boundary condition was derived by using a general three-dimensional curvilinear coordinate system. Here, x_1, x_2, and x_3 are the computational domain axes and u_1, u_2, and u_3 are the corresponding velocities. At each cell face, a local Cartesian coordinate system (X_1, X_2, and X_3) is established by the inward normal of that cell face and two other linearly independent directions in the plane of the cell face. A velocity vector in this neighborhood is decomposed into vector components in the local coordinate system. Across this boundary, a ghost point b is assumed to be located at the mirror image of the real point p within the computational domain. (See fig. A(1).) The velocity vector associated with the ghost point is the mirror image of the original velocity vector and satisfies the following condition:

$$\begin{Bmatrix} U_1 \\ U_2 \\ U_3 \end{Bmatrix}^b = \begin{Bmatrix} -U_1 \\ U_2 \\ U_3 \end{Bmatrix}^p \tag{A1}$$

where U_i is related to the local velocities u_i for points p and b through the $\mathbf{A}$ (transformation) matrix,

$$\left.\begin{aligned} \mathbf{U}^b &= \mathbf{A}u^b \\ \mathbf{U}^p &= \mathbf{A}u^p \end{aligned}\right\} \tag{A2}$$

where

$$\left.\begin{aligned} \mathbf{A} &= \begin{bmatrix} n_1 & n_2 & n_3 \\ m_1 & m_2 & m_3 \\ l_1 & l_2 & l_3 \end{bmatrix} \\ \mathbf{A}^{-1} &= \mathbf{A}^T \end{aligned}\right\} \tag{A3}$$

and n, m, and l are the directional cosines between the X and x coordinates. Equation (A2) can be rewritten from equations (A1) and (A3) as follows:

$$\begin{aligned} u^b &= \mathbf{A}^{-1}\mathbf{U}^b \\ &= \mathbf{A}^{-1}\left(\mathbf{U}^p - 2U_1\{1,0,0\}^T\right) \\ &= \mathbf{A}^{-1}\mathbf{A}u^p - 2\mathbf{U}_1\mathbf{A}^T\{1,0,0\}^T \end{aligned}$$

Furthermore, the above equation can be written in the simpler form,

$$u^b = u^p - 2\mathbf{U}_1\{n_1, n_2, n_3\}^T \tag{A4}$$

Special Cases

Halfplane Symmetry

In the case of halfplane symmetry, the symmetry plane is aligned with the x_1–x_3 plane and the $\mathbf{N}$ array is defined as

$$\mathbf{N} = \{0,1,0\}^T$$

Substituting the values for $\mathbf{N}$ in equations (A2) and (A4) yields

$$\begin{Bmatrix} u_1 \\ u_2 \\ u_3 \end{Bmatrix}^b = \begin{Bmatrix} u_1 \\ -u_2 \\ u_3 \end{Bmatrix}^p$$

Quarterplane Symmetry

In the case of quarterplane symmetry, two symmetry planes exist. One is the same as the halfplane symmetry case; the other symmetry plane is aligned with the x_2, x_3 plane. The $\mathbf{N}$ array is defined as

$$\mathbf{N} = \{1,0,0\}^T$$

Substituting the values for $\mathbf{N}$ in equations (A2) and (A4) yields

$$\begin{Bmatrix} u_1 \\ u_2 \\ u_3 \end{Bmatrix}^b = \begin{Bmatrix} -u_1 \\ u_2 \\ u_3 \end{Bmatrix}^p$$

This mathematical formulation is implemented in the PAB3D Navier-Stokes code and replaces all the special cases of symmetry boundary conditions. It is also used for specifying a slip boundary condition for Euler flow calculations. The halfplane symmetry for a polar grid is an exception to this rule. The velocity vector image is reflected across the halfplane boundary, whereas the ghost points at the pole are reflected across a moving mirror. Nevertheless, the generalized symmetry boundary condition can be easily modified to work in this case, and it has been included in the PAB3D code. This generalized symmetry condition has tremendously simplified the boundary condition procedure in advanced Navier-Stokes and Euler CFD methods. It also provides the ability to include symmetry boundary conditions in a structured CFD grid without the restrictions for alignment with the global coordinate system.

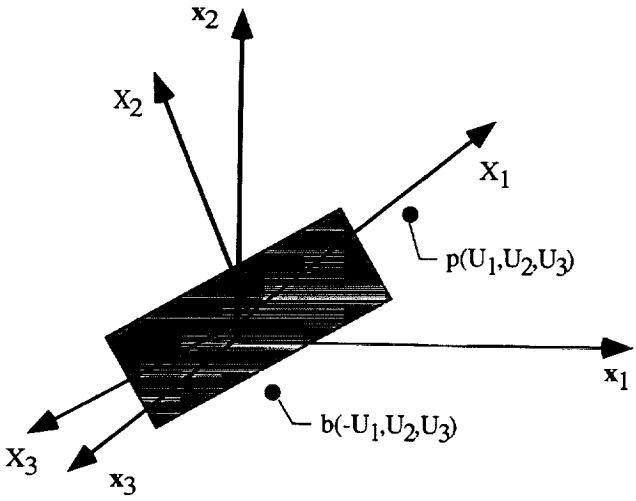

$$\begin{Bmatrix} u_1 \\ u_2 \\ u_3 \end{Bmatrix}^b = \begin{Bmatrix} u_1 \\ u_2 \\ u_3 \end{Bmatrix}^p - 2U_1 \begin{Bmatrix} n_1 \\ n_2 \\ n_3 \end{Bmatrix} \quad (U_1 = n_i u_i)$$

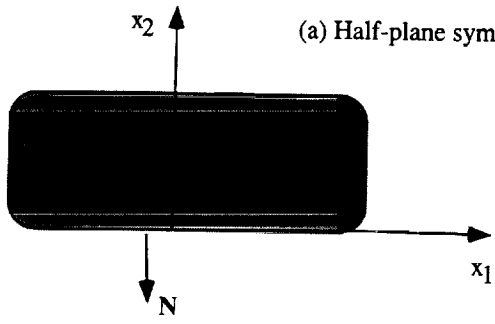

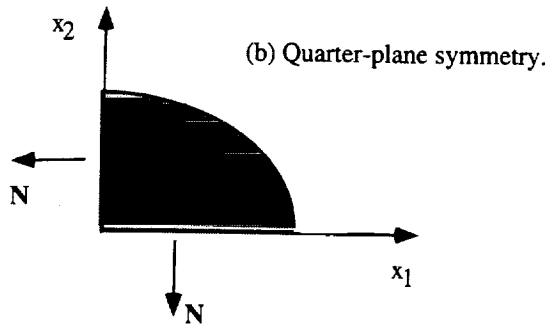

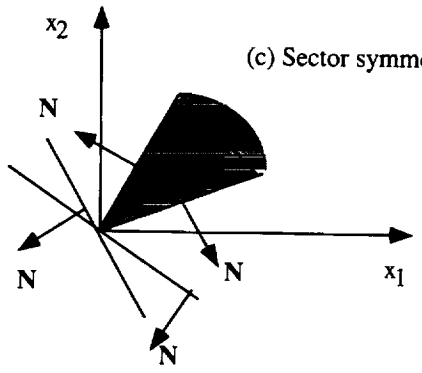

Figure A1. Symmetry boundary condition formulated in local Cartesian coordinate system.

References

1. Jones, W. P.; and Launder, B. E.: The Prediction of Laminarization With a Two-Equation Model of Turbulence. *Int. J. Heat & Mass Transf.*, vol. 15, no. 2, Feb. 1972, pp. 301–314.

2. Launder, B. E.; Reece, G. J.; and Rodi, W.: Progress in the Development of a Reynolds-Stress Turbulence Closure. *J. Fluid Mech.*, vol. 68, pt. 3, Apr. 1975, pp. 537–566.

3. Sarkar, S.; and Lakshmanan, B.: Application of a Reynolds Stress Turbulence Model to the Compressible Shear Layer. *AIAA J.*, vol. 29, no. 5, May 1991, pp. 743–749.

4. Moin, Parviz; and Kim, John: Numerical Investigation of Turbulent Channel Flow. *J. Fluid. Mech.*, vol. 118, 1982, pp. 341–377.

5. Speziale, Charles G.: On Nonlinear K-l and K-ϵ Models of Turbulence. *J. Fluid Mech.*, vol. 178, 1987, pp. 459–475.

6. Sarkar, S.; Erlebacher, G.; Hussaini, M. Y.; and Kreiss, H. O.: The Analysis and Modeling of Dilatational Terms in Compressible Turbulence. *J. Fluid Mech.*, vol. 227, June 1991, pp. 473–495.

7. Wilcox, David C.: Progress in Hypersonic Turbulence Modeling. AIAA-91-1785, June 1991.

8. Abdol-Hamid, Khaled S.: Application of a Multiblock/ Multizone Code (PAB3D) for the Three-Dimensional Navier-Stokes Equations. AIAA-91-2155, June 1991.

9. Abdol-Hamid, Khaled S.; Uenishi, K.; Keith, B. D.; and Carlson, John R.: Commercial Turbofan Engine Exhaust Nozzle Flow Analyses. *J. Propuls. & Power*, vol. 9, no. 3, May–June 1993, pp. 431–436.

10. Pao, S. Paul; Carlson, John R.; and Abdol-Hamid, Khaled S.: Computational Investigation of Circular-to-Rectangular Transition Ducts. *J. Propuls. & Power*, vol. 10, no. 1, Jan.–Feb. 1994, pp. 95–100.

11. Rubesin, Morris W.; Maydew, Randall C.; and Varga, Steven A.: *An Analytical and Experimental Investigation of the Skin Friction of the Turbulent Boundary Layer on a Flat Plate at Supersonic Speeds.* NACA TN 2305, 1951.

12. Settles, Gary S.; Vas, Irwin E.; and Bogdonoff, Seymour M.: Details of a Shock-Separated Turbulent Boundary Layer at a Compression Corner. *AIAA J.*, vol. 14, no. 12, Dec. 1976, pp. 1709–1715.

13. Cook, P. H.; McDonald, M. A.; and Firmin, M. C. P.: Aerofoil RAE 2822—Pressure Distributions and Boundary Layer and Wake Measurements. *Experimental Data Base for Computer Program Assessment*, AGARD-AR-138, May 1979, pp. A6-1–A6-77.

14. Gessner, F. B.; Ferguson, S. D.; and Lo, C. H.: Experiments on Supersonic Turbulent Flow Development in a Square Duct. *AIAA J.*, vol. 25, no. 5, May 1987, pp. 690–697.

15. Baldwin, Barrett; and Lomax, Harvard: Thin-Layer Approximation and Algebraic Model for Separated Turbulent Flows. AIAA-78-257, Jan. 1978.

16. Nagano, Y.; and Hishida, M.: Improved Form of the K-ϵ Model for Wall Turbulent Shear Flow. *J. Fluid Mech.*, vol. 109, June 1987, pp. 156–160.

17. Speziale, Charles G.; Abid, Ridha; and Anderson, E. Clay: A Critical Evaluation of Two-Equation Models for Near Wall Turbulence. AIAA-90-1481, June 1990.

18. Kook, Myong Hyon; and Kobayashi, Toshio: Prediction of Three-Dimensional Developing Turbulent Flow in a Square Duct With an Anisotropic Low-Reynolds-Number k-ϵ Model. *J. Fluids Eng.*, vol. 113, no. 4, Dec. 1991, pp. 608–615.

19. Carlson, John R.: *A Nozzle Internal Performance Prediction Method.* NASA TP-3221, 1992.

20. Carlson, John R.: *Computational Prediction of Isolated Performance of an Axisymmetric Nozzle at Mach Number 0.90.* NASA TM-4506, 1994.

21. Ames Res. Staff: *Equations, Tables, and Charts for Compressible Flow.* NACA Rep. 1135, 1953.

22. Thangam, S.; and Speziale, C. G.: Turbulent Flow Past a Backward-Facing Step: A Critical Evaluation of Two-Equation Models. *AIAA J.*, vol. 30, no. 5, May 1992, pp. 1314–1320.

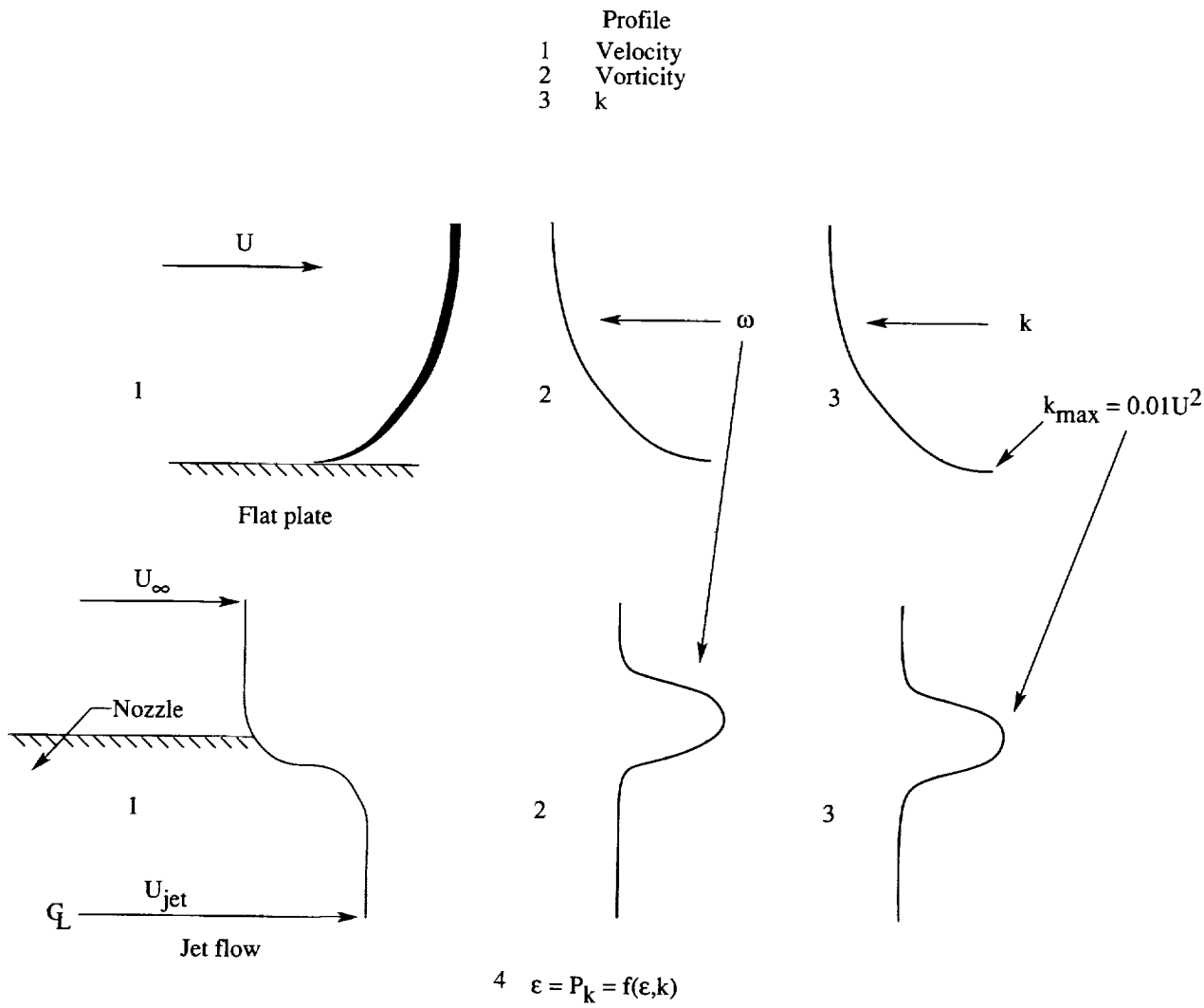

Figure 1. Inflow boundary condition for k-ε turbulence model.

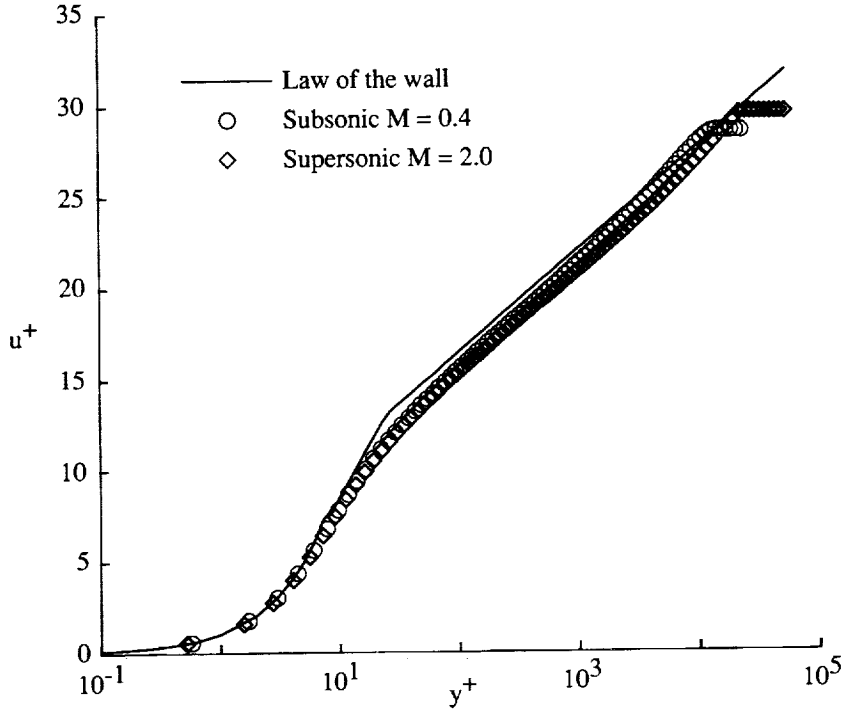

Figure 2. Solution for subsonic and supersonic flows with k-ε1 over flat-plate boundary layer.

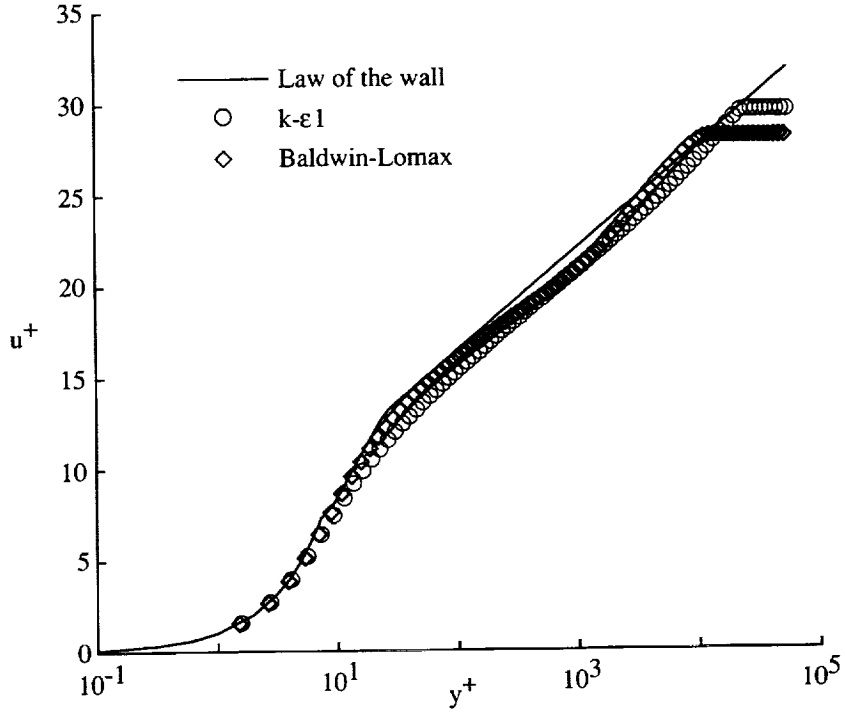

Figure 3. Solution for supersonic flow over flat-plate boundary layer based on k-ε1 and Baldwin-Lomax models.

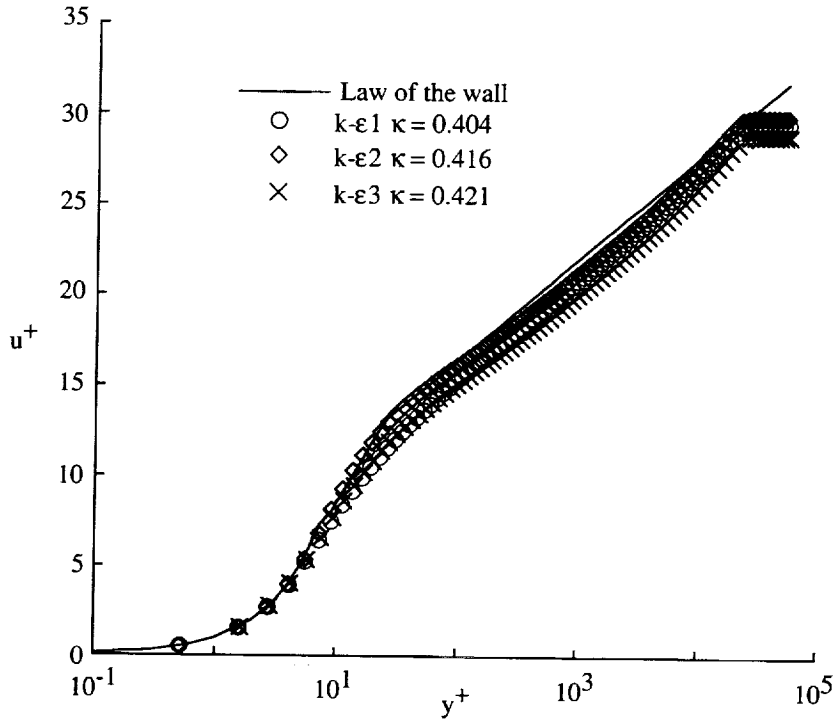

Figure 4. Solution for supersonic flow over flat-plate boundary layer based on k-$\varepsilon 1$, k-$\varepsilon 2$, and k-$\varepsilon 3$ models.

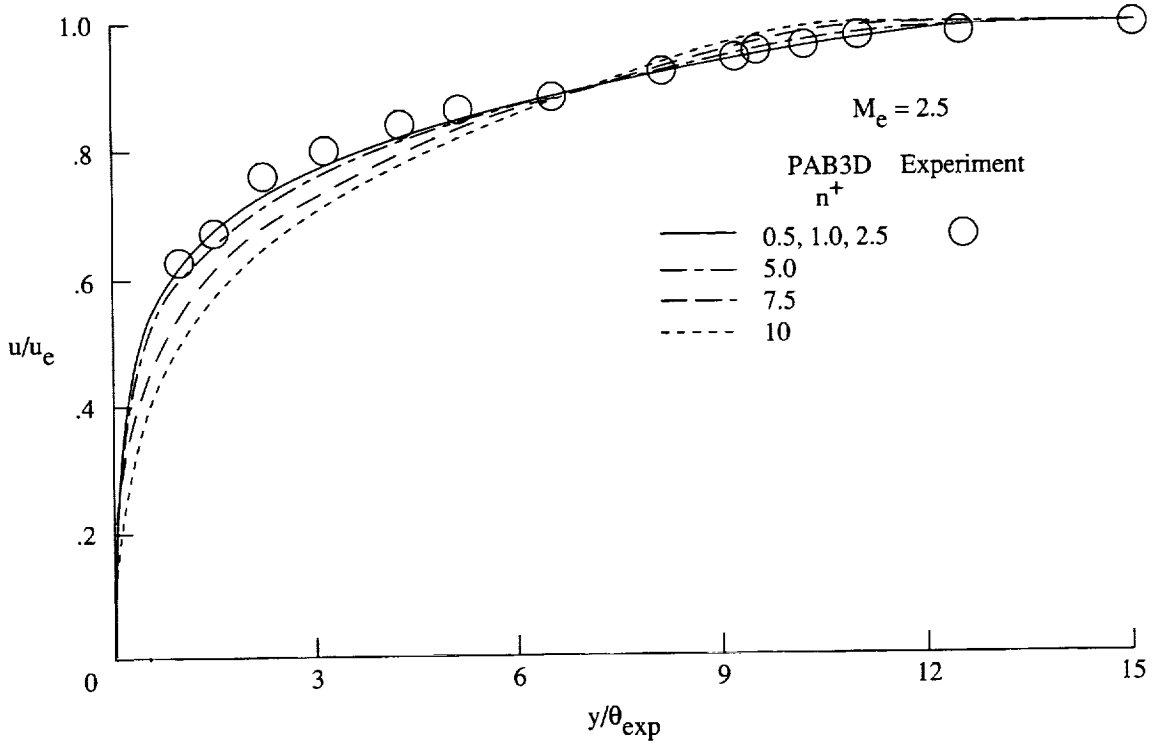

(a) k-ε1 turbulence model.

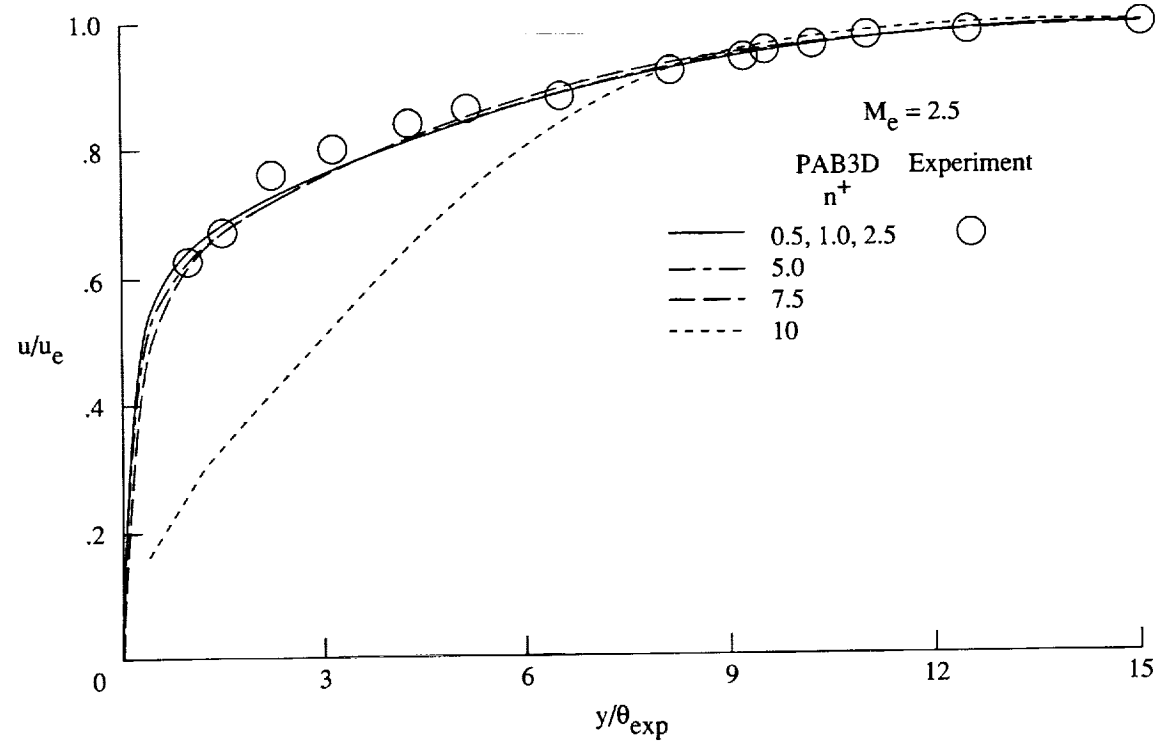

(b) Baldwin-Lomax turbulence model.

Figure 5. Effect of spacing first grid point off wall on velocity profile.

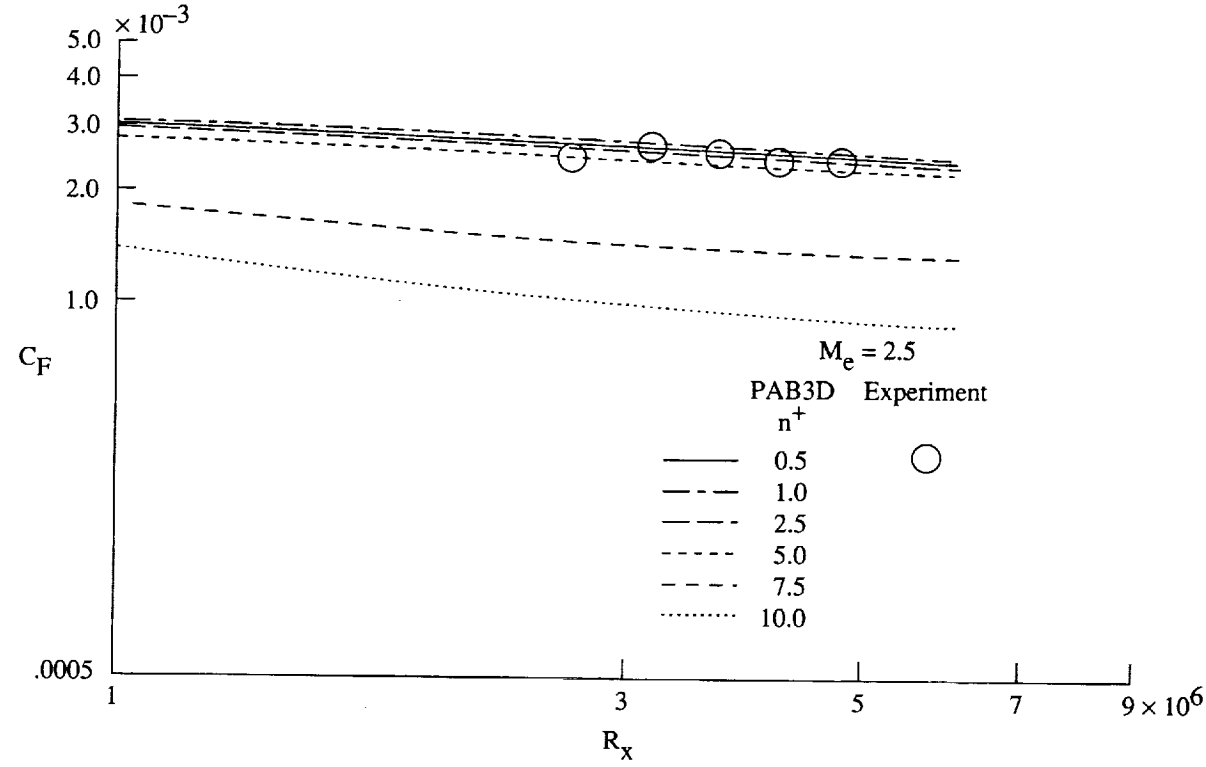

(a) k-ε1 turbulence model.

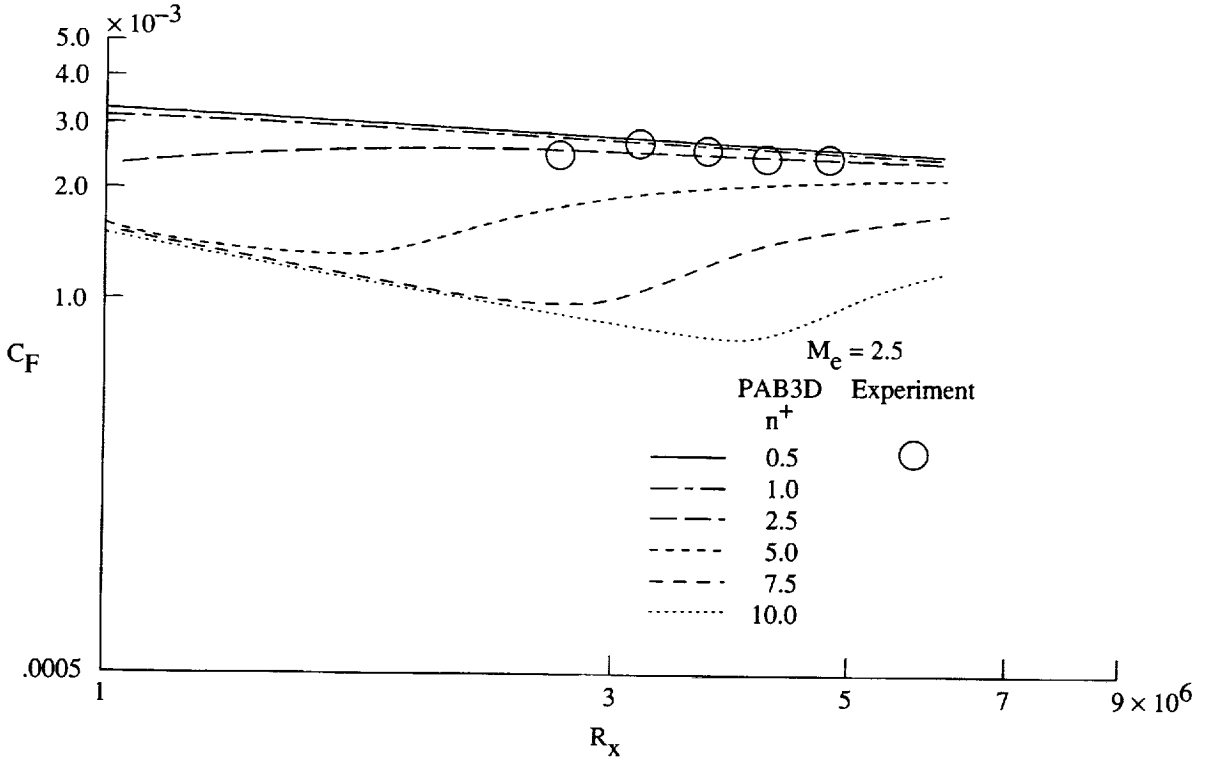

(b) Baldwin-Lomax turbulence model.

Figure 6. Effect of spacing first grid point off wall on average skin-friction distribution.

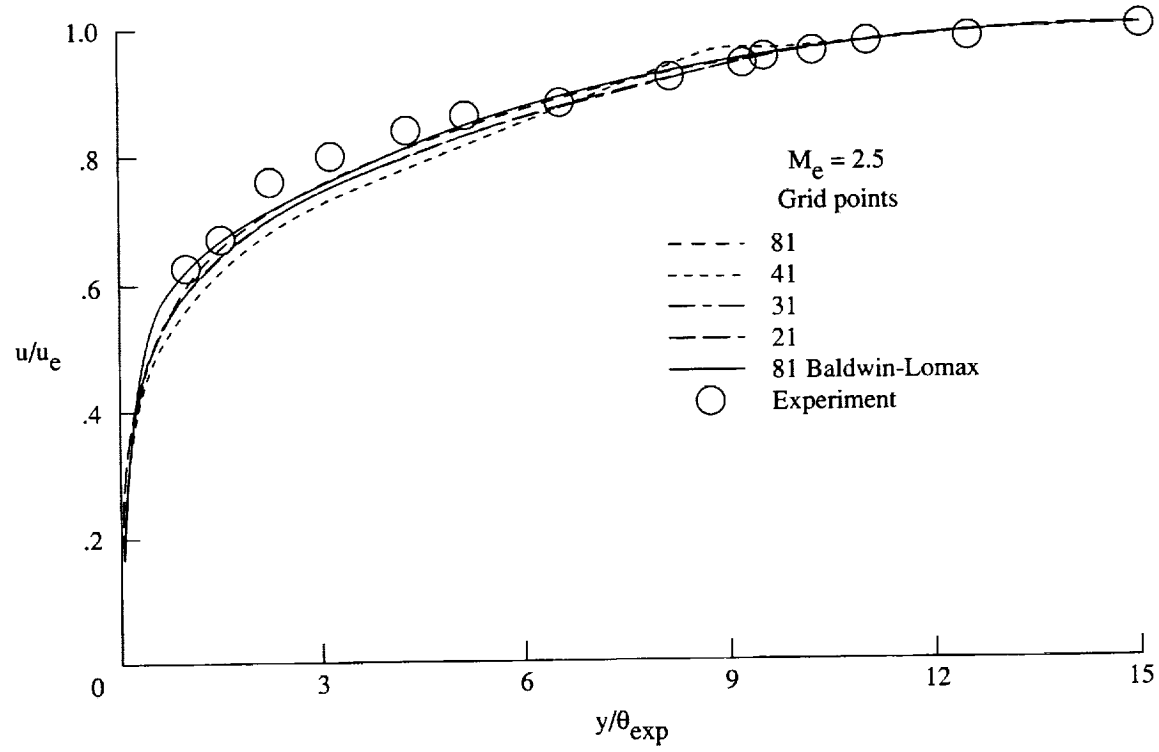

(a) Velocity profile.

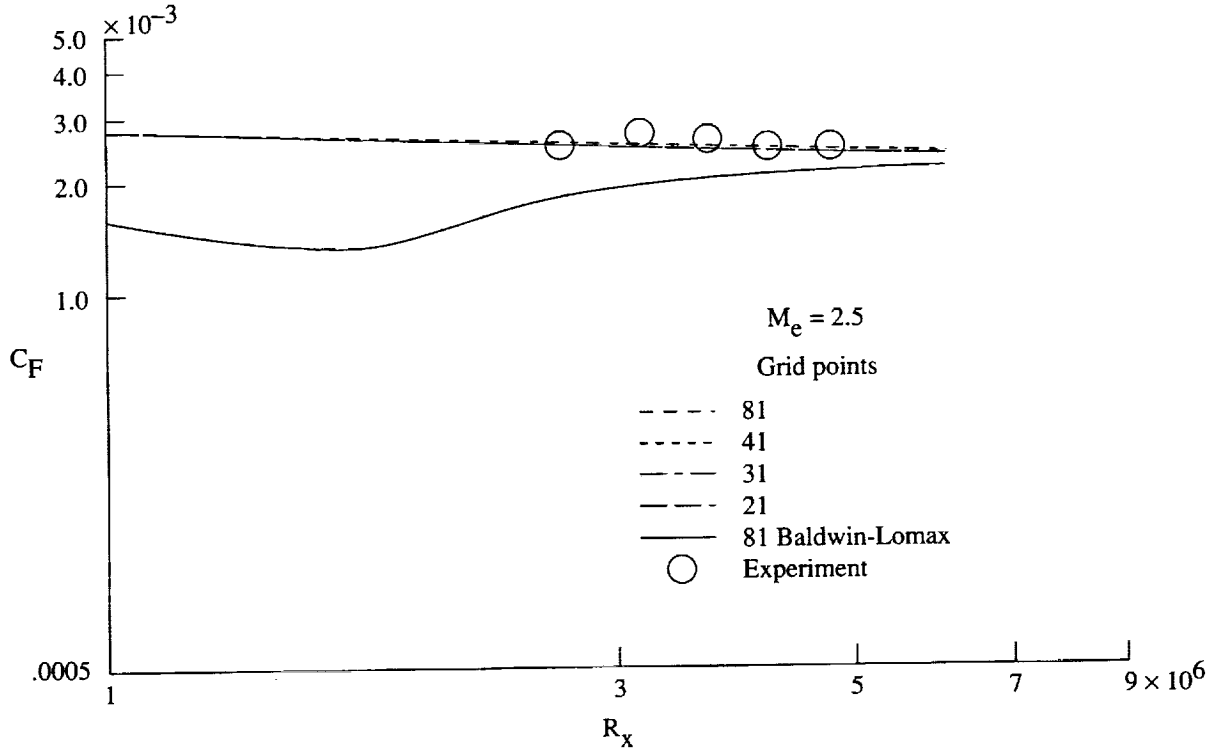

(b) Average skin-friction distribution.

Figure 7. Effect of grid distribution in normal direction with k-ε turbulence model for $n^+ = 5$.

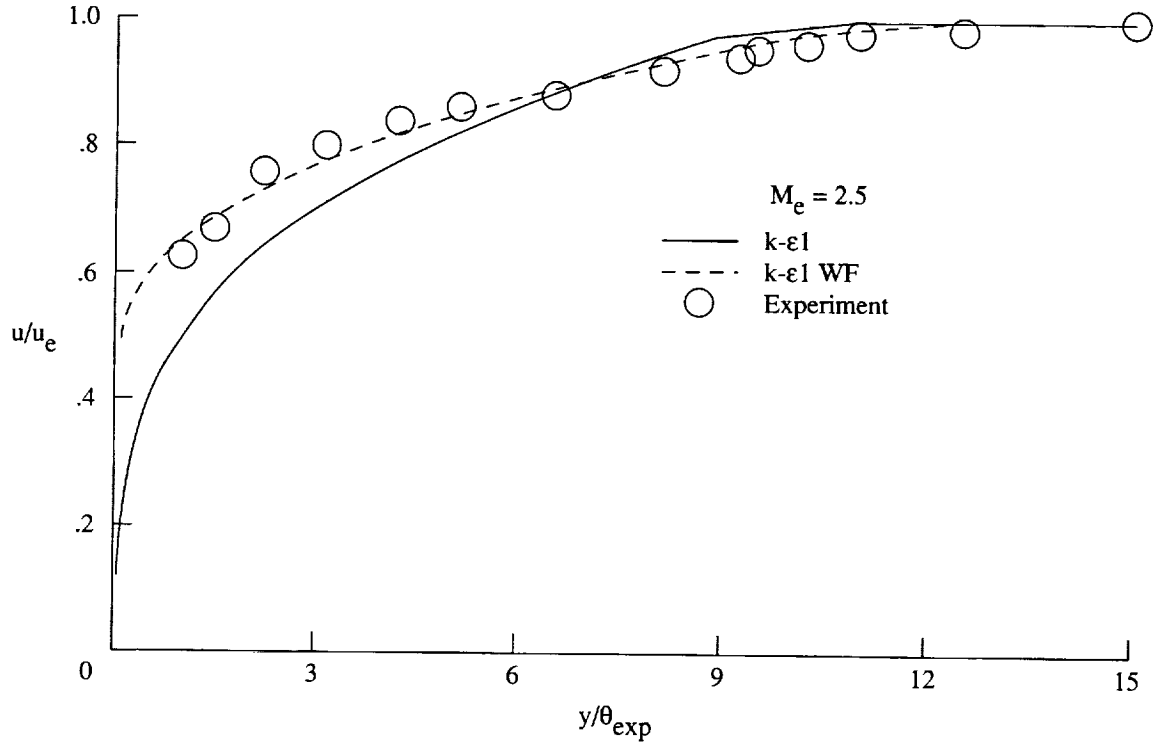

(a) Velocity profile.

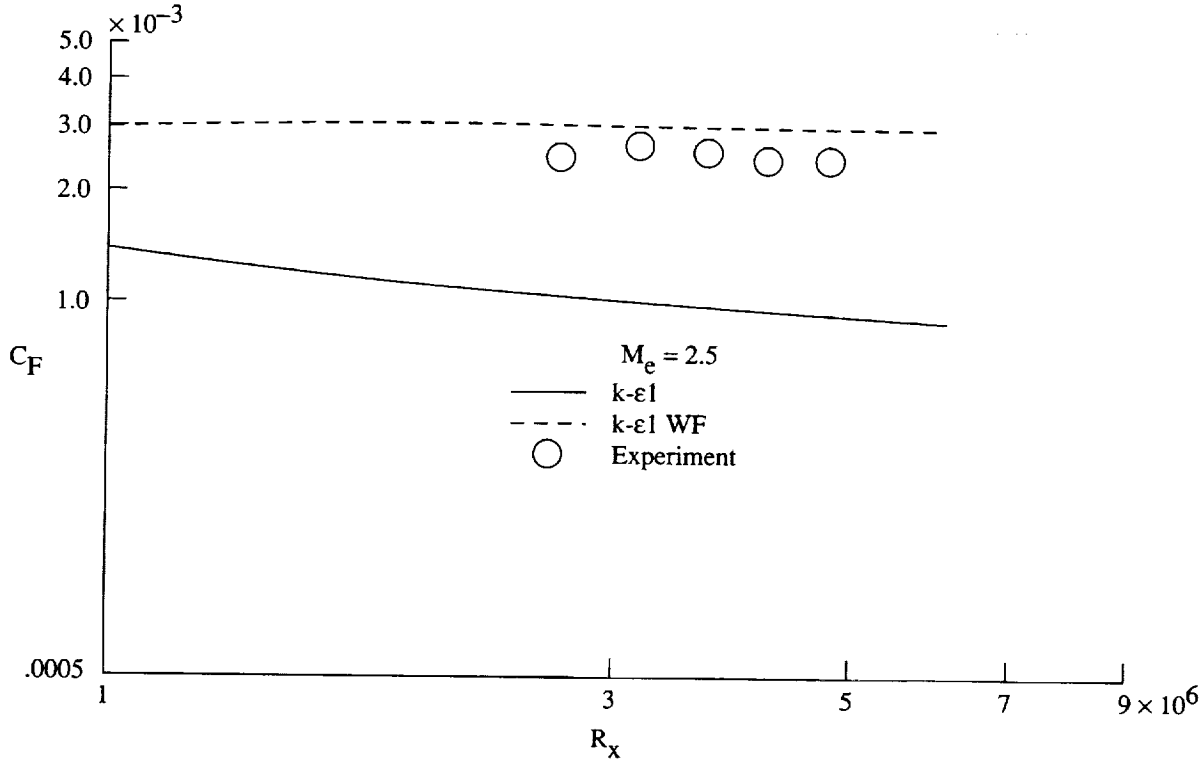

(b) Average skin-friction distribution.

Figure 8. Solution for k-ε model with and without wall function for $n^+ = 10$.

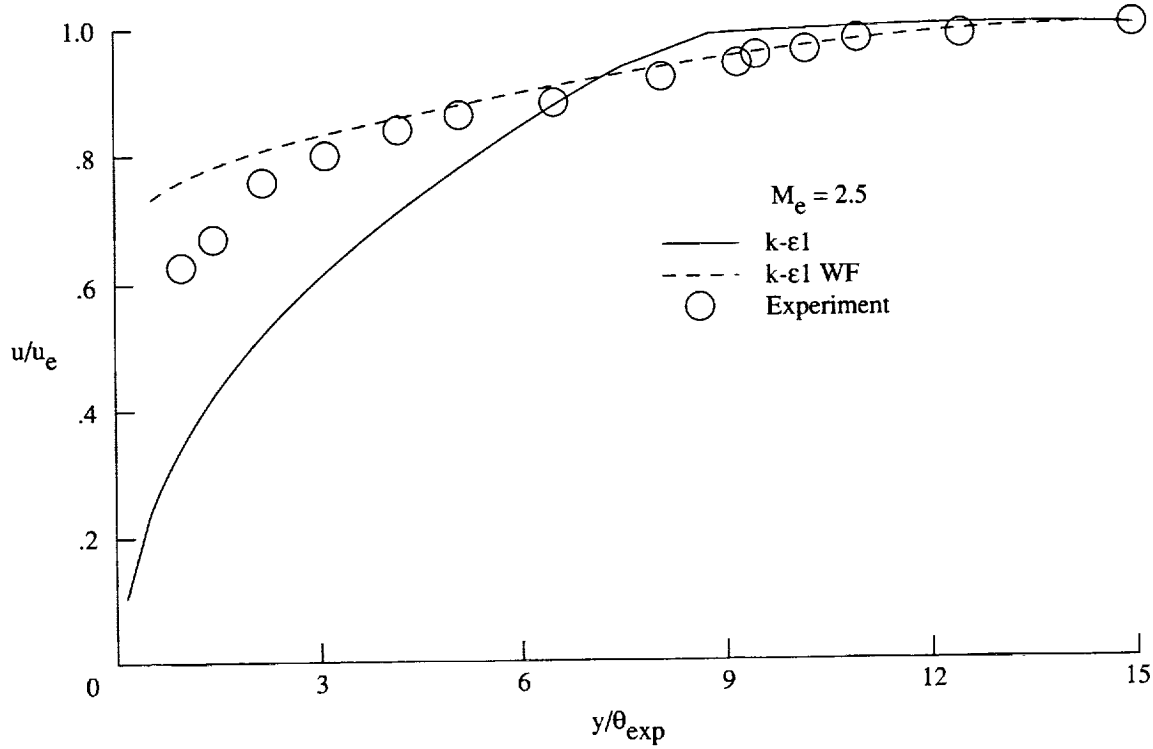

(a) Velocity profile.

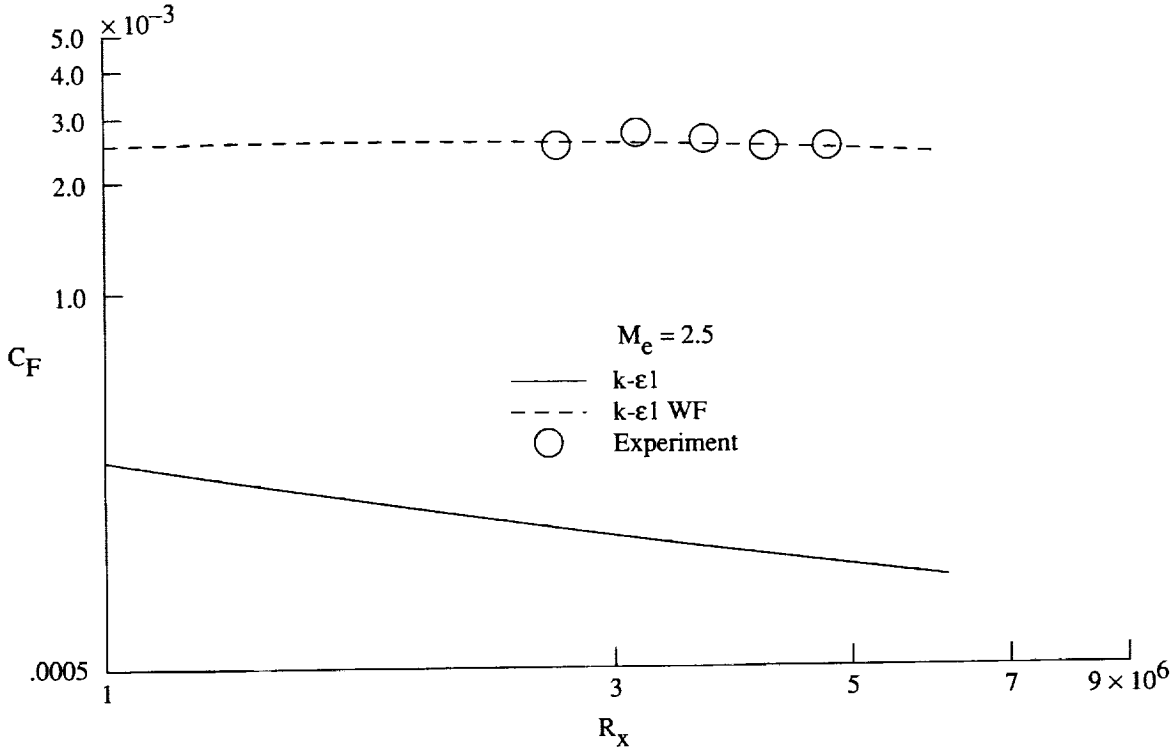

(b) Average skin-friction distribution.

Figure 9. Solution for k-ε model with and without wall functions for $n^+ = 50$.

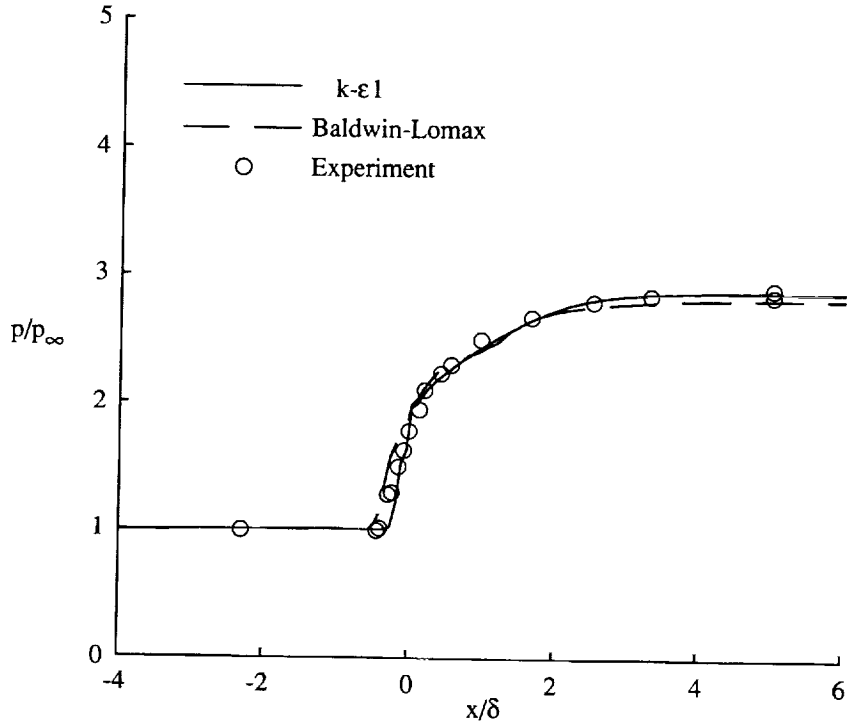

(a) Wall pressure distribution.

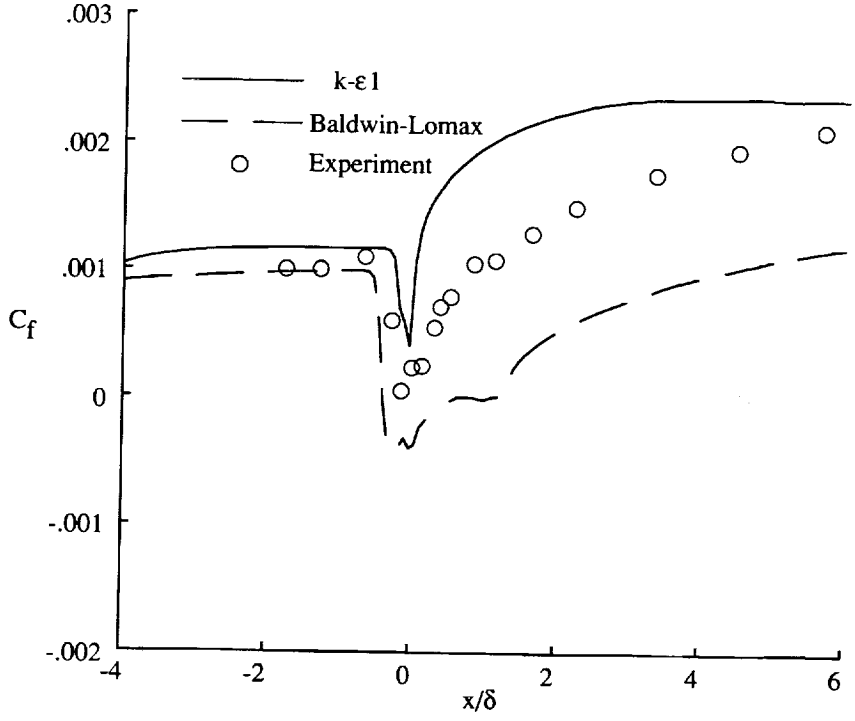

(b) Skin-friction distribution.

Figure 10. Computations for 16° compression ramp with Baldwin-Lomax and k-ε1 models.

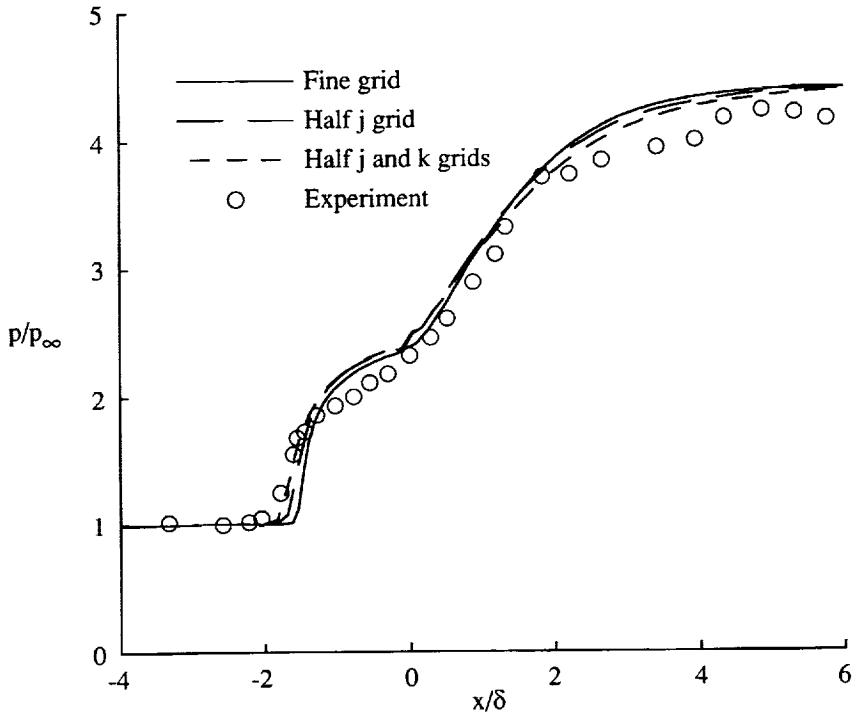

(a) Wall pressure distribution.

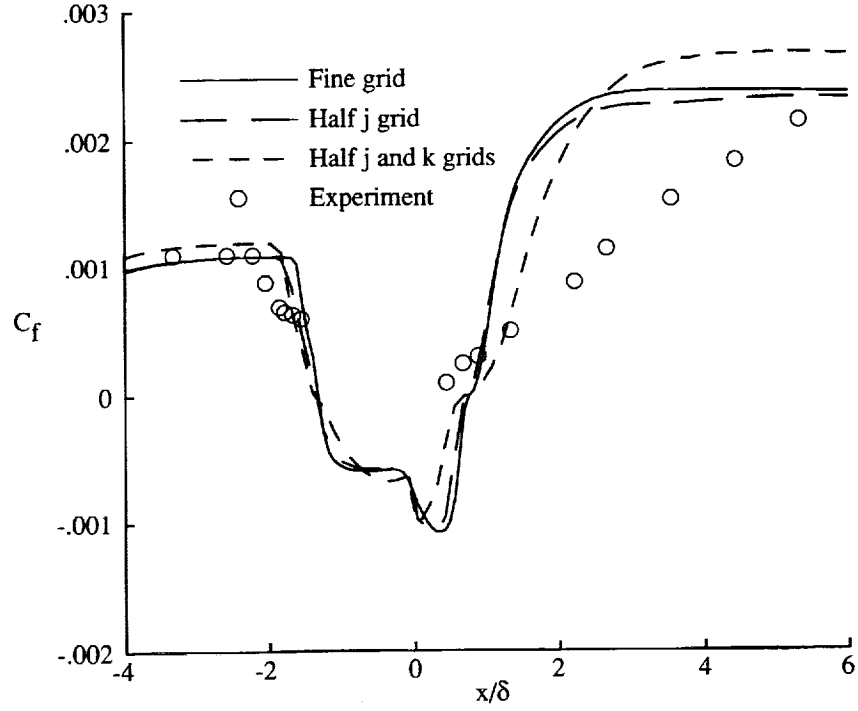

(b) Skin-friction distribution.

Figure 11. Computations for 24° compression ramp for k-ε1 models with different grid resolutions.

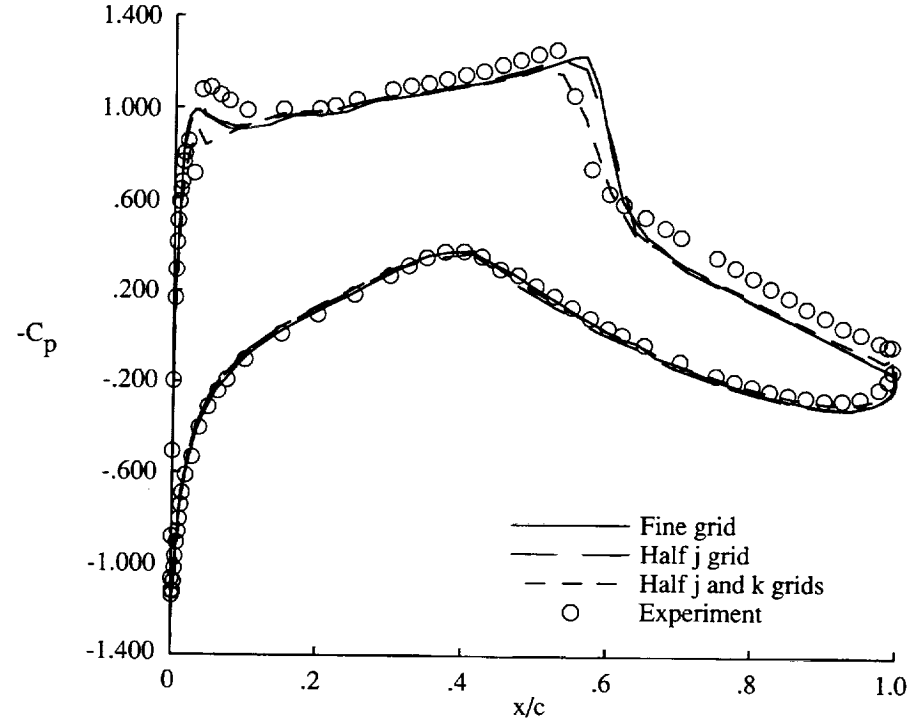

(a) Pressure distribution.

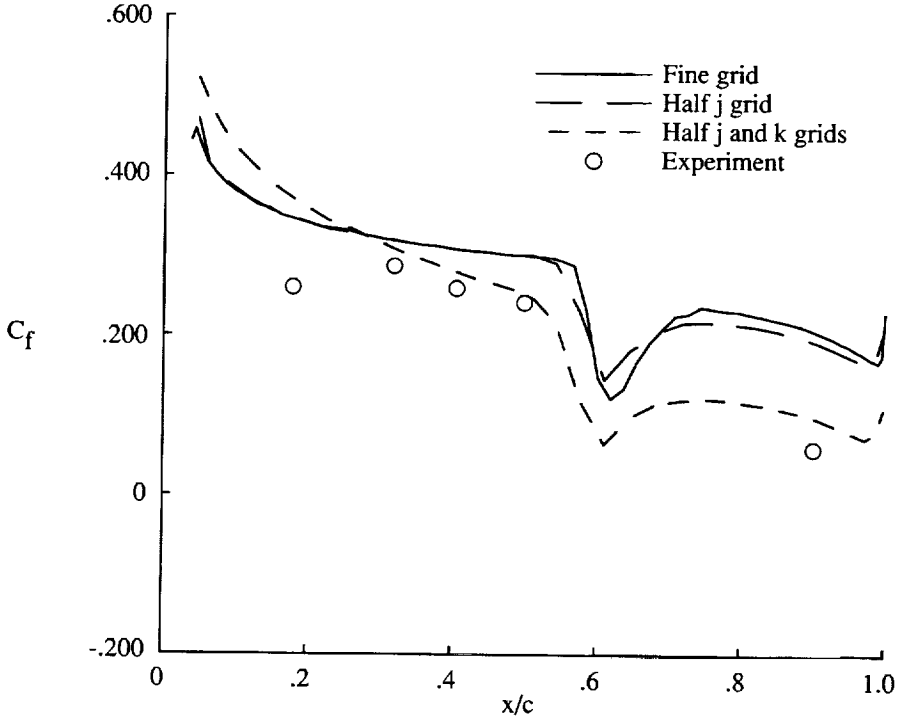

(b) Local skin-friction distribution.

Figure 12. Effect of grid for two-dimensional airfoil section with k-ε1 turbulence model.

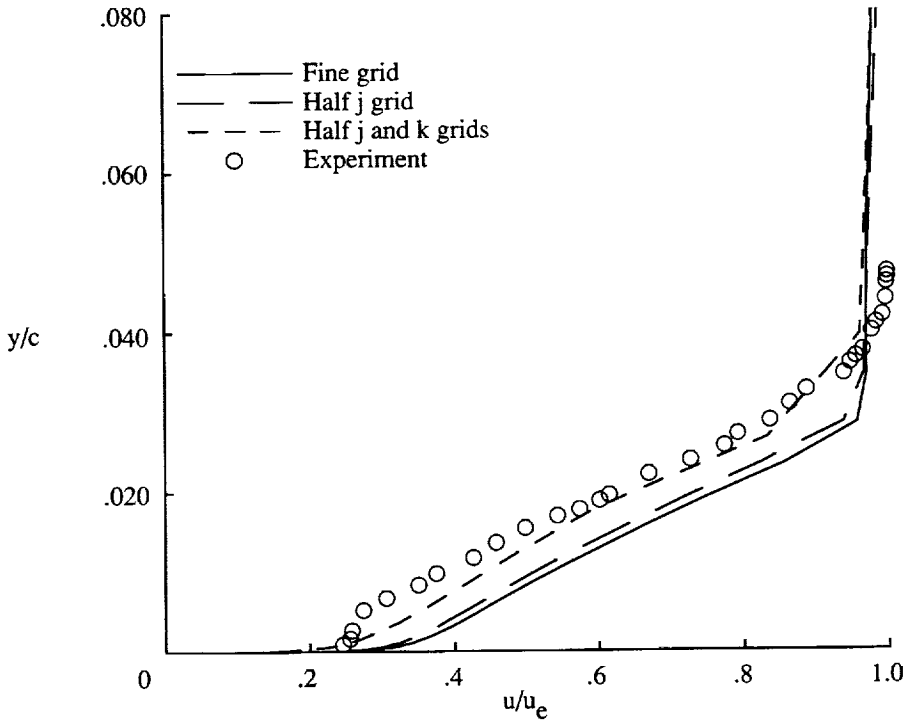

(c) Velocity profile.

Figure 12. Concluded.

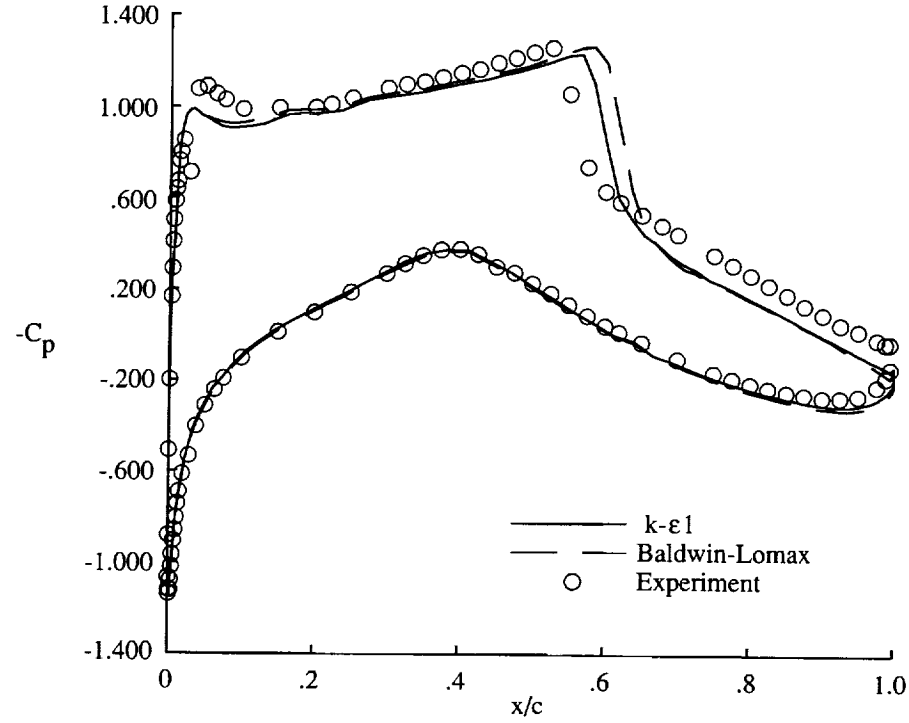

(a) Pressure distribution.

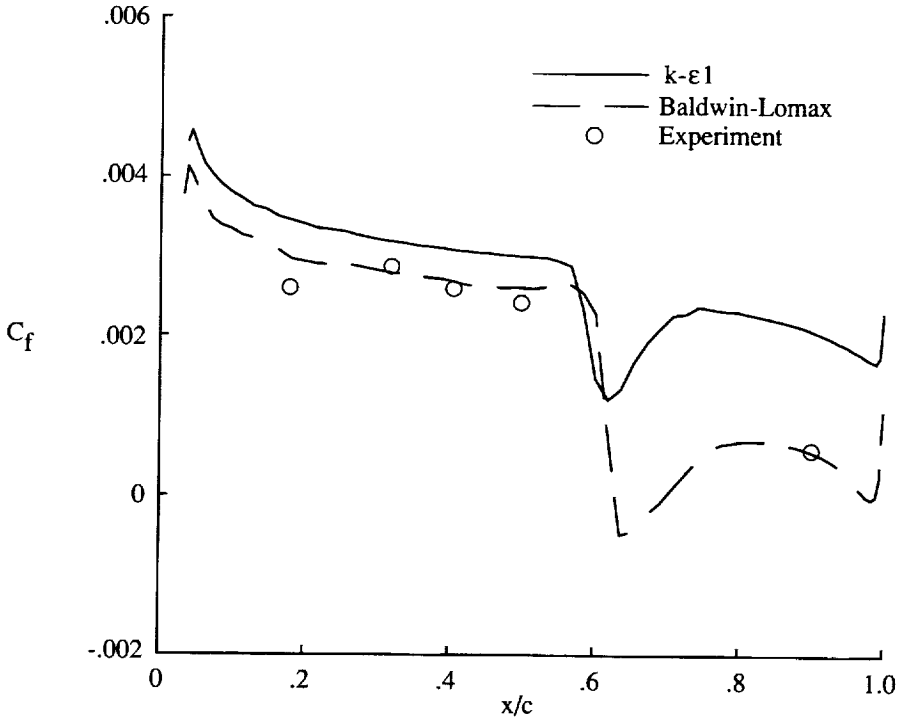

(b) Local skin-friction distribution.

Figure 13. Computations for two-dimensional airfoil section with Baldwin-Lomax and k-ε1 turbulence models.

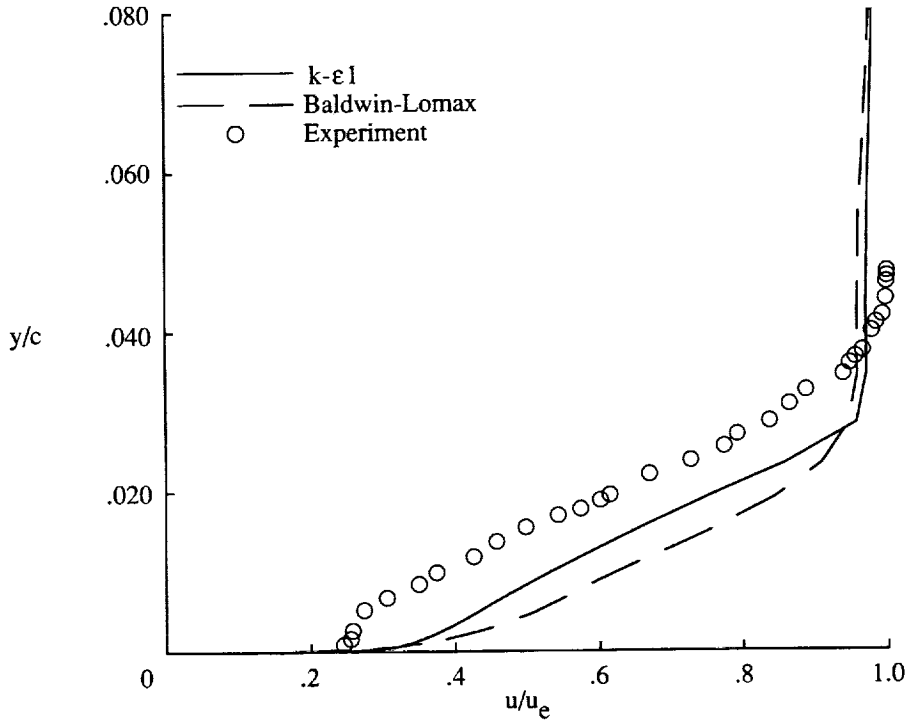

(c) Velocity profile for $x/c = 0.9$.

Figure 13. Concluded.

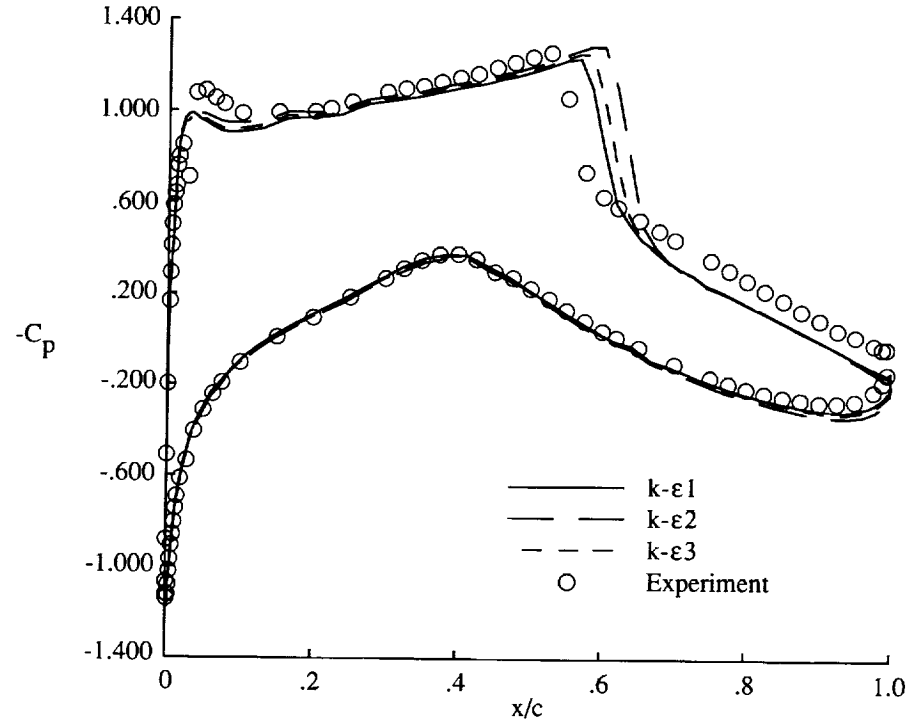

(a) Pressure distribution.

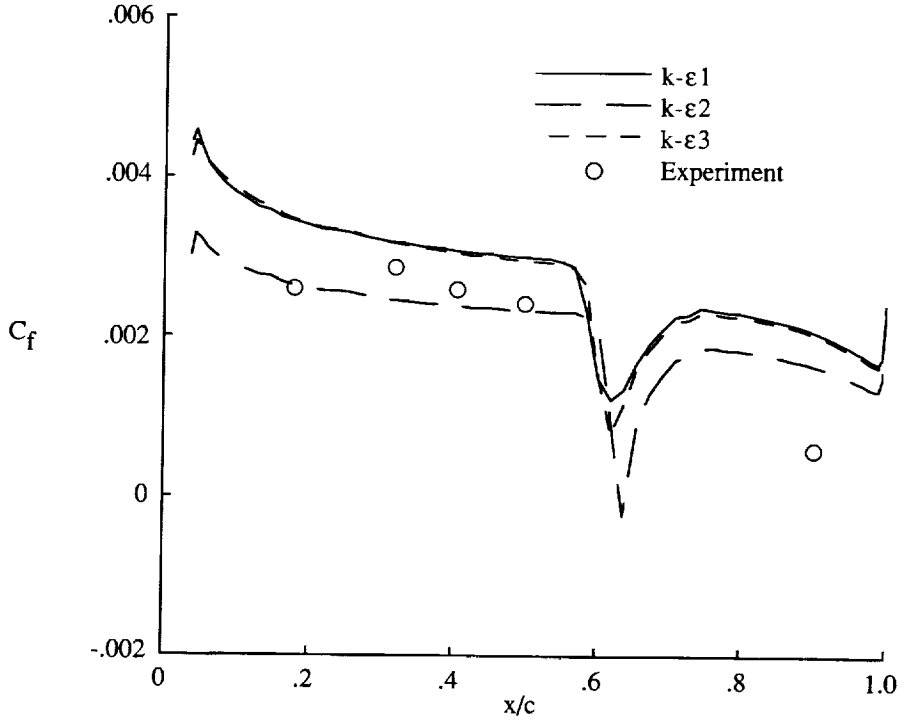

(b) Local skin-friction distribution.

Figure 14. Computations for two-dimensional airfoil section with Baldwin-Lomax and k-ε1 turbulence models.

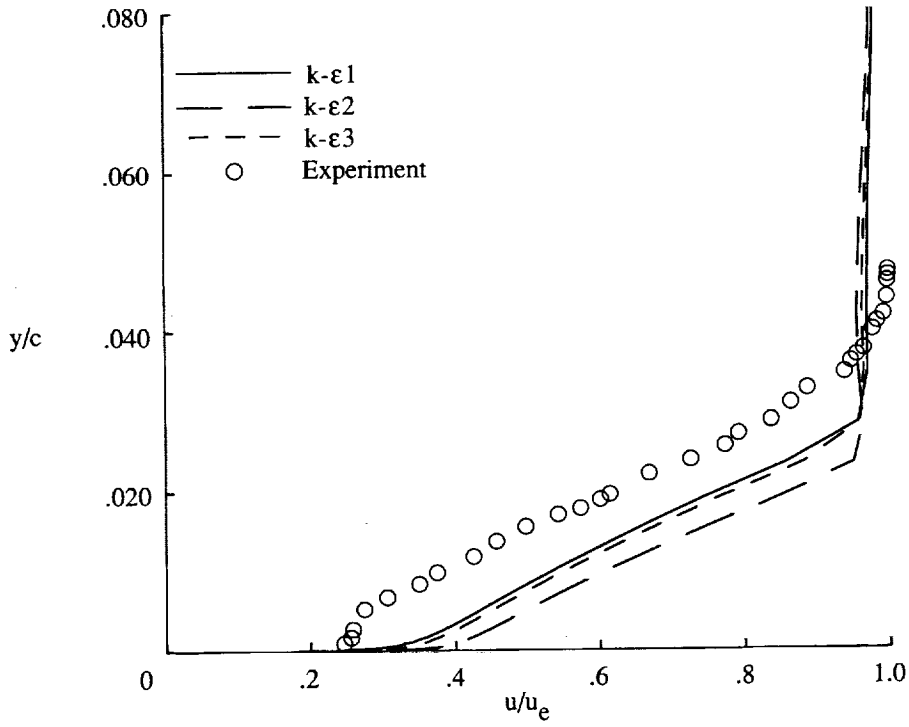

(c) Velocity profile for $x/c = 0.9$.

Figure 14. Concluded.

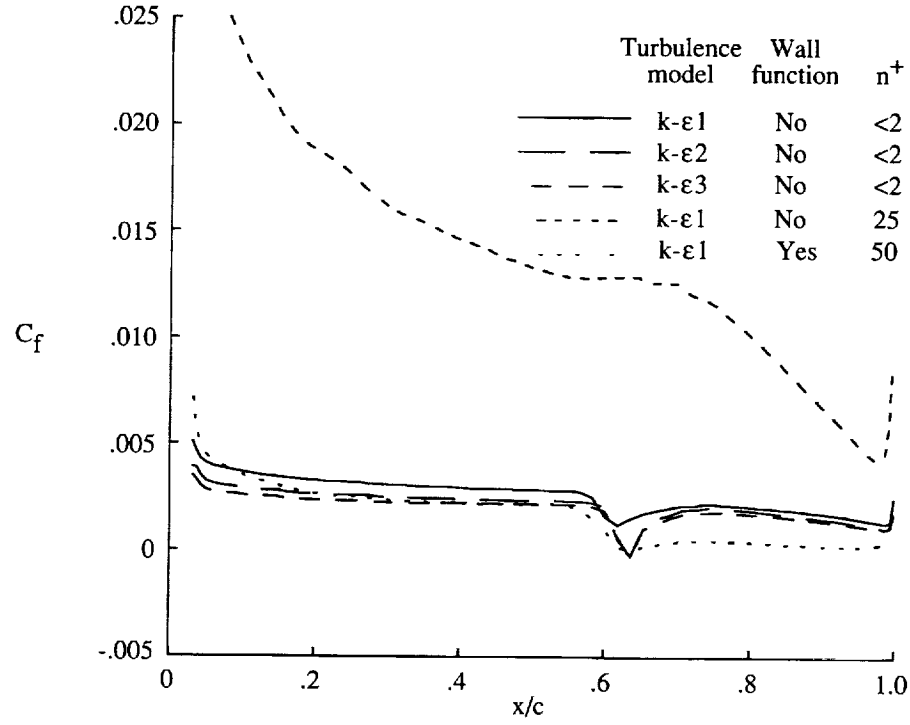

Figure 15. Local skin-friction distribution for two-dimensional airfoil section for different forms of k-ε turbulence models with and without wall function.

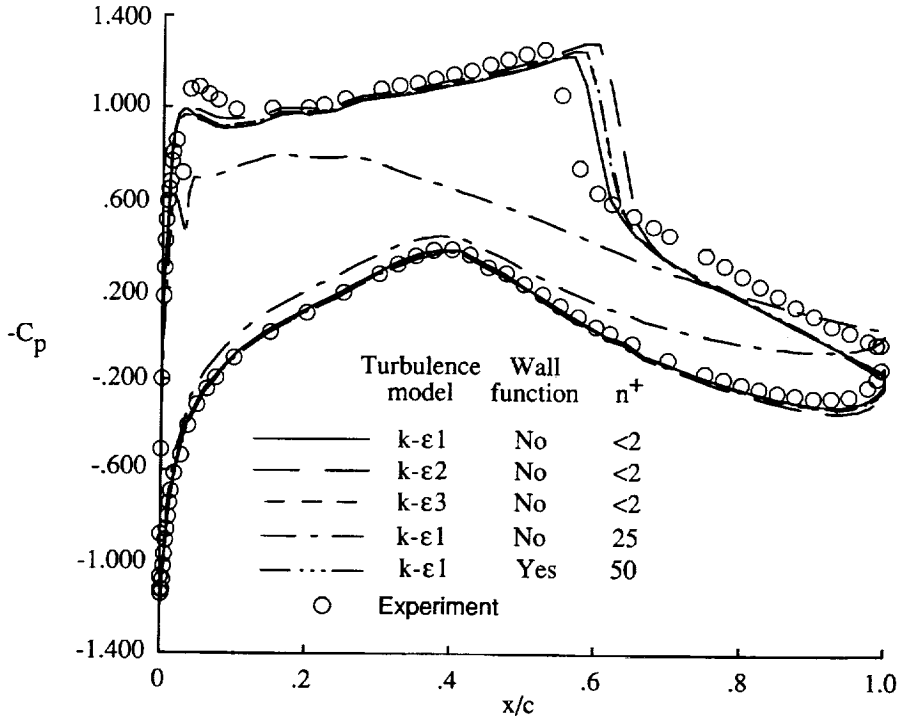

Figure 16. Wall pressure distribution for two-dimensional airfoil section for different forms of k-ε turbulence models with and without wall function.

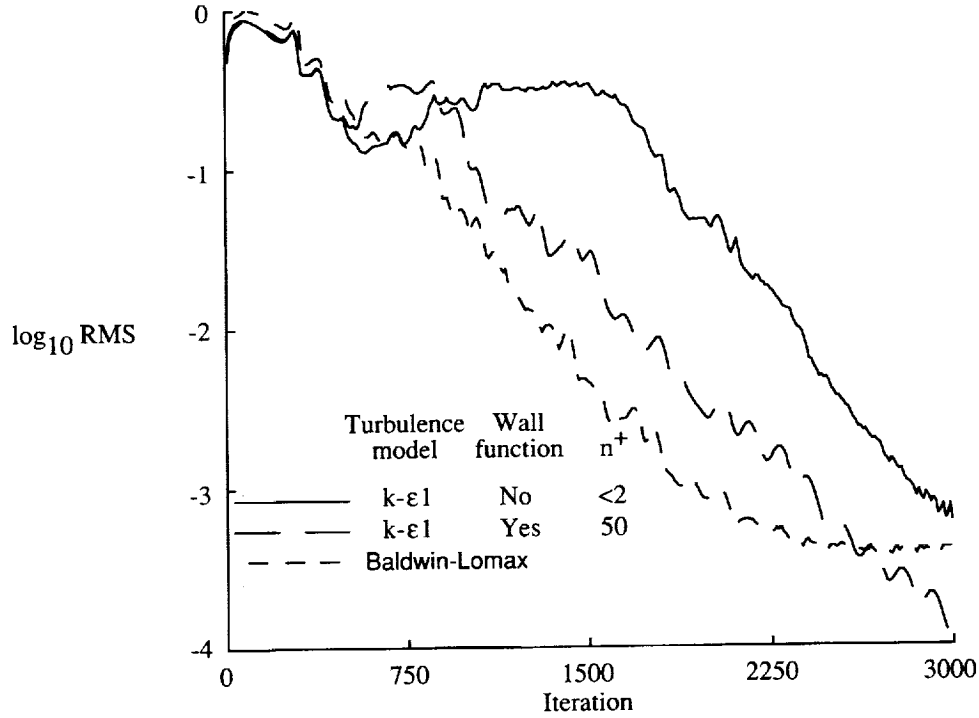

Figure 17. Convergence history for k-ε1 with and without wall function and Baldwin-Lomax turbulence models.

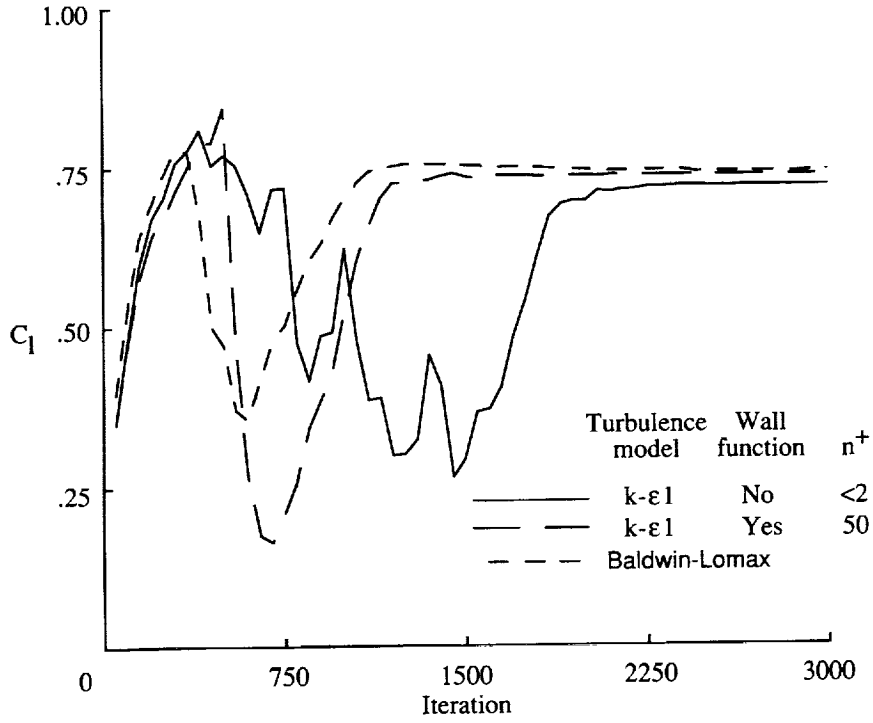

Figure 18. Lift coefficient for k-ε1 with and without wall function and Baldwin-Lomax turbulence models.

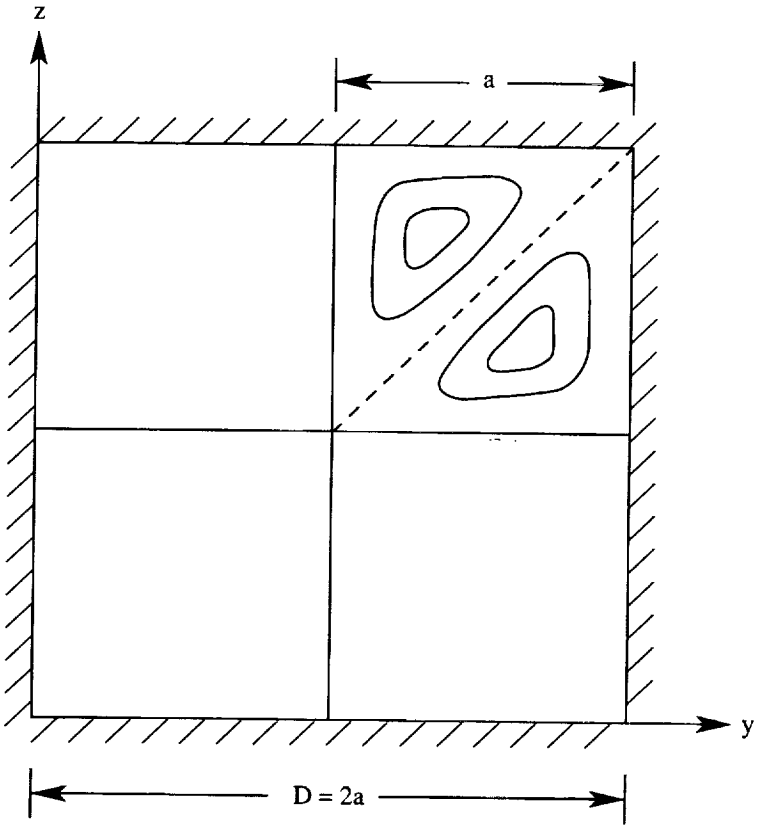

Figure 19. Secondary flow in square duct.

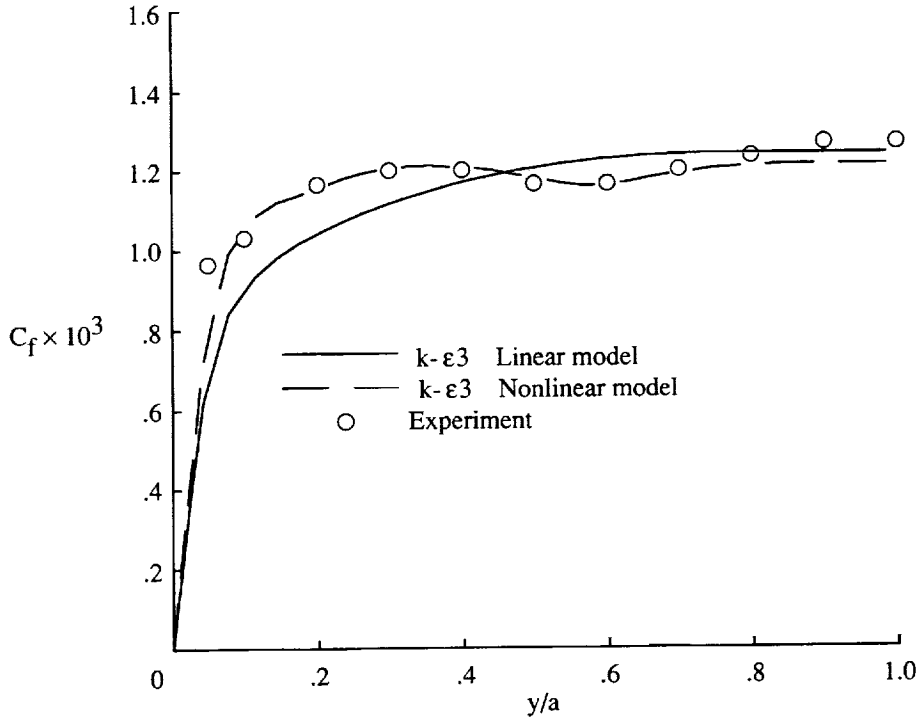

Figure 20. Local skin-friction distribution with linear and nonlinear models for supersonic flow through square duct.

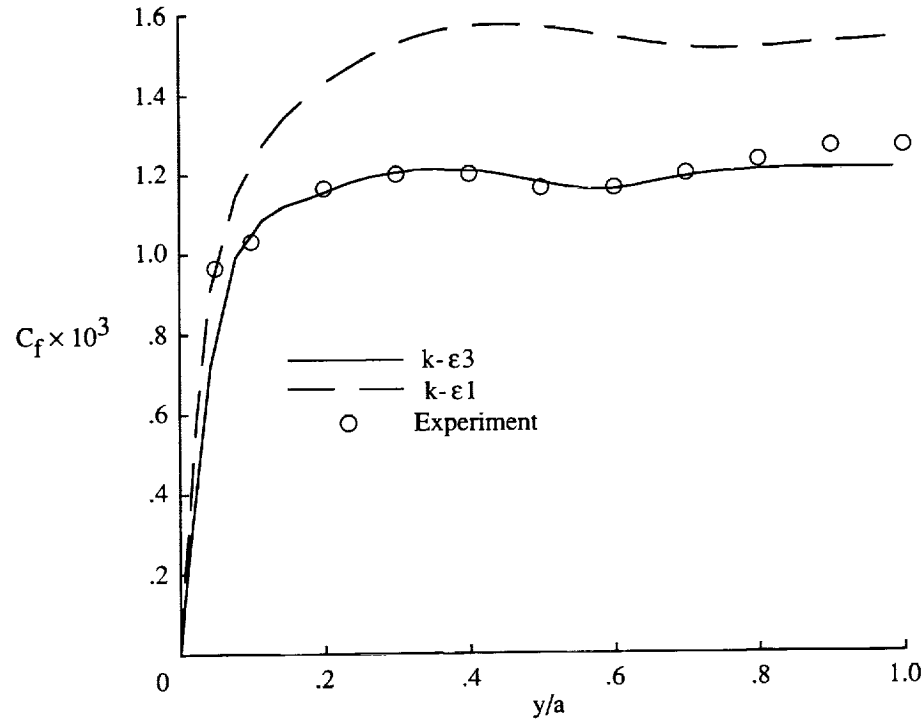

Figure 21. Effect of near-wall terms on nonlinear model for supersonic flow through square duct.

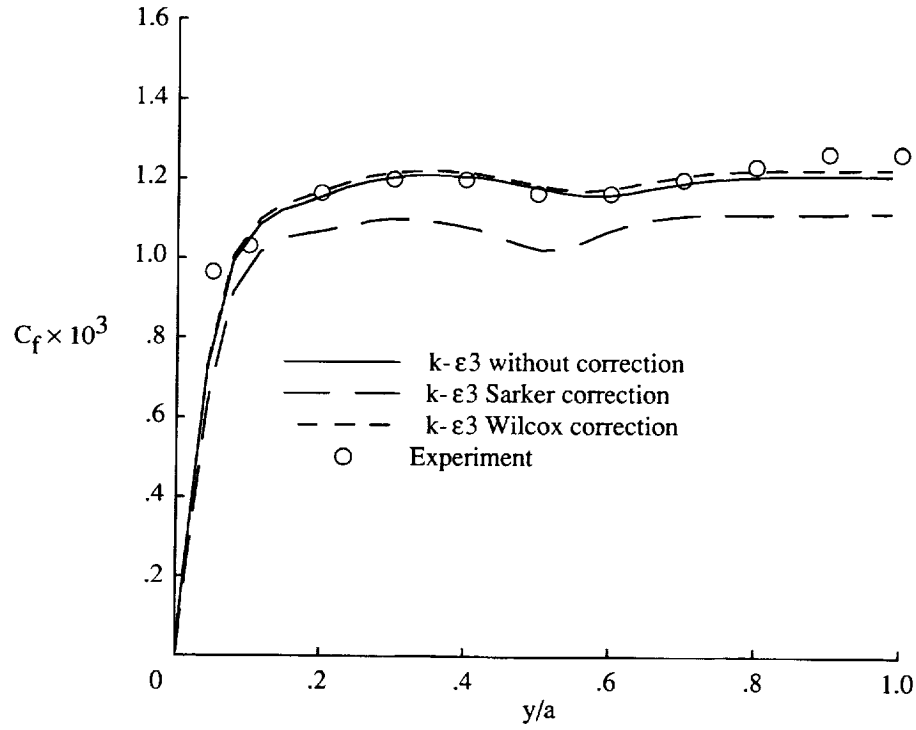

Figure 22. Effect of compressibility correction on nonlinear model for supersonic flow through square duct.

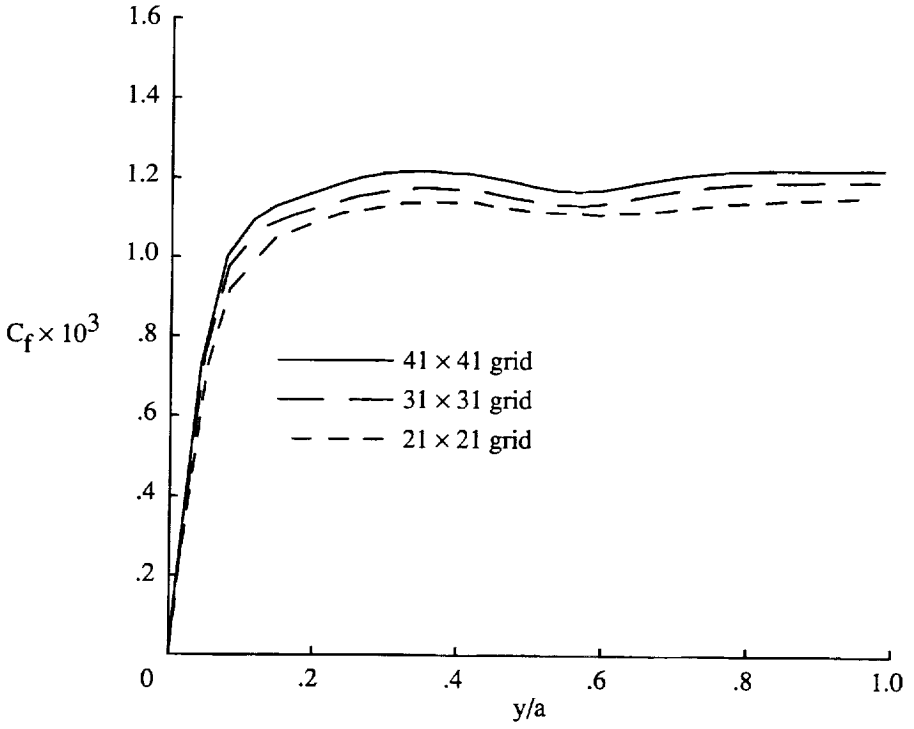

Figure 23. Effect of grid resolution and k-ε3 model on nonlinear model for supersonic flow through square duct.

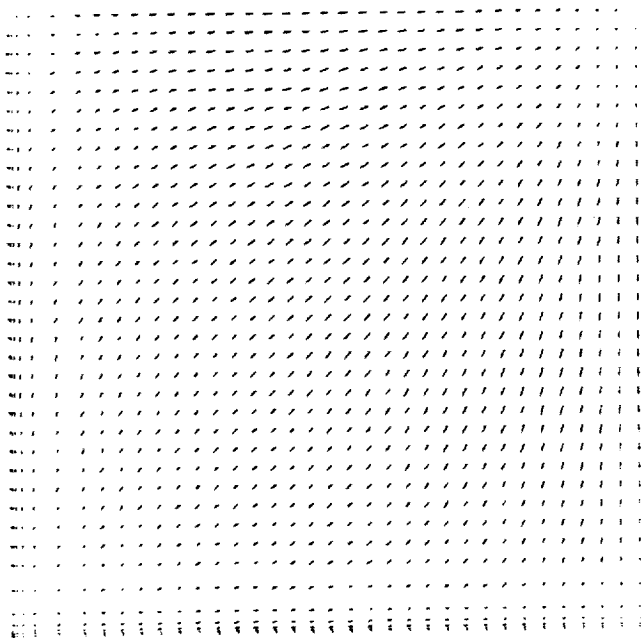

(a) Linear model.

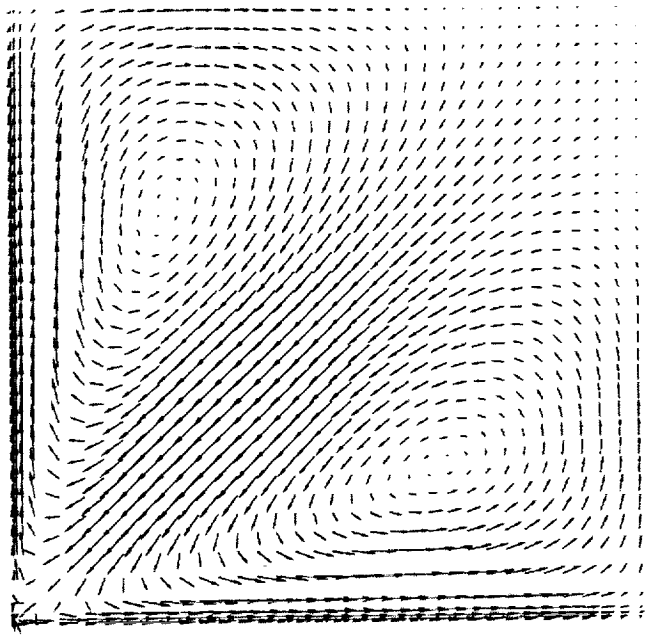

(b) Nonlinear model.

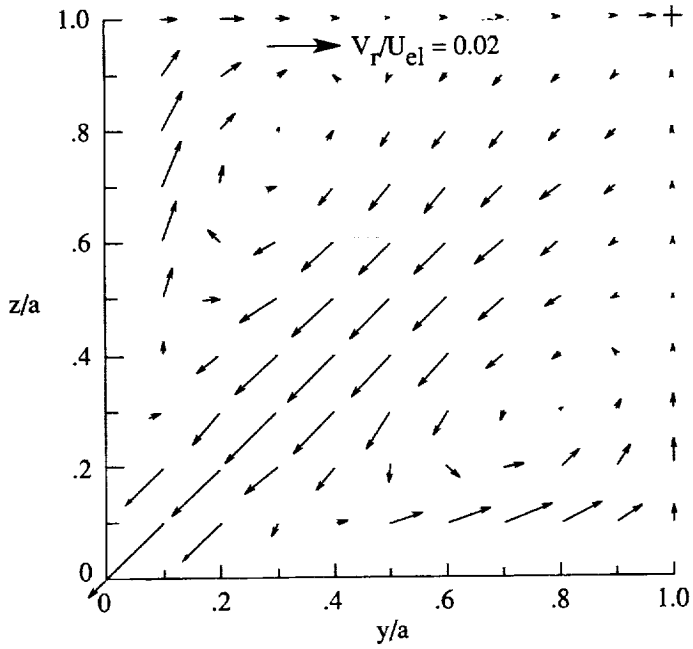

(c) Experiment.

Figure 24. Cross-flow velocity patterns at $x/D = 50$ for supersonic flow through square duct; computed with k-ε3 model.

REPORT DOCUMENTATION PAGE

Form Approved
OMB No. 0704-0188

1. AGENCY USE ONLY *(Leave blank)*	2. REPORT DATE	3. REPORT TYPE AND DATES COVERED
	January 1995	Technical Paper

4. TITLE AND SUBTITLE
Application of Navier-Stokes Code PAB3D With k-ϵ Turbulence Model to Attached and Separated Flows

5. FUNDING NUMBERS
WU 505-59-10-20

6. AUTHOR(S)
Khaled S. Abdol-Hamid, B. Lakshmanan, and John R. Carlson

7. PERFORMING ORGANIZATION NAME(S) AND ADDRESS(ES)
NASA Langley Research Center
Hampton, VA 23681-0001

8. PERFORMING ORGANIZATION REPORT NUMBER
L-17354

9. SPONSORING/MONITORING AGENCY NAME(S) AND ADDRESS(ES)
National Aeronautics and Space Administration
Washington, DC 20546-0001

10. SPONSORING/MONITORING AGENCY REPORT NUMBER
NASA TP-3480

11. SUPPLEMENTARY NOTES
Abdol-Hamid: Analytical Services & Materials, Inc., Hampton, VA; Lakshmanan: Old Dominion University, Norfolk, VA; Carlson: Langley Research Center, Hampton, VA.

12a. DISTRIBUTION/AVAILABILITY STATEMENT
Unclassified–Unlimited
Subject Category 02
Availability: NASA CASI (301) 621-0390

12b. DISTRIBUTION CODE

13. ABSTRACT *(Maximum 200 words)*
A three-dimensional Navier-Stokes solver was used to determine how accurately computations can predict local and average skin friction coefficients for attached and separated flows for simple experimental geometries. Algebraic and transport equation closures were used to model turbulence. To simulate anisotropic turbulence, the standard two-equation turbulence model was modified by adding nonlinear terms. The effects of both grid density and the turbulence model on the computed flow fields were also investigated and compared with available experimental data for subsonic and supersonic free-stream conditions.

14. SUBJECT TERMS
Computational fluid dynamics; Navier-Stokes; Turbulence models; Two-equation k-ϵ; Near-wall model; Supersonic flows; Separated flows; Multiblock

15. NUMBER OF PAGES
41

16. PRICE CODE
A03

17. SECURITY CLASSIFICATION OF REPORT	18. SECURITY CLASSIFICATION OF THIS PAGE	19. SECURITY CLASSIFICATION OF ABSTRACT	20. LIMITATION OF ABSTRACT
Unclassified	Unclassified	Unclassified	